Monte Carlo Simulations of the Background and Performance of the Future Satellite Observatories eXTP and HERMES

Masterarbeit

am Institut für Astronomie und Astrophysik
der Eberhard Karls Universität Tübingen

vorgelegt von

Sarah Sauter

Juli 2019

Hiermit versichere ich, Sarah Sauter, dass ich die vorliegende Masterarbeit selbständig verfasst und keine anderen als die angegebenen Hilfsmittel und Quellen benutzt habe. Die wörtlich oder sinngemäß aus anderen Werken übernommenen Aussagen sind als solche gekennzeichnet und diese Arbeit ist weder vollständig noch in wesentlichen Teilen zuvor veröffentlicht oder bei einer anderen Prüfungsbehörde eingereicht worden.

Ort, Datum

Unterschrift

Abstract

Since mostly faint X-ray sources are detected in the presence of a strong background in space, there is a great interest in minimizing the influence of this background on the observation. The background caused by interactions of high energy cosmic particles with the observatory significantly limits the sensitivity that can be achieved with the instrument. Thus, sources below a minimum detectable flux cannot be detected. Therefore, it is important to keep the detector background as low as possible.

This work is concerned with Monte Carlo simulation studies to predict the detector background of future X-ray observatories. First, a suitable simulation environment was created and validation studies were performed using the simulation toolkit Geant4.

With its four scientific instruments, the planned X-ray observatory eXTP is well suited for the study of black holes, neutron stars and magnetars, which provide an insight into matter under extreme conditions such as in very strong gravitational and magnetic fields and in supranuclear density conditions. In this work, simulation studies on the detector background of eXTP's Large Area Detector instrument were performed, for which a suitable detector geometry had to be developed. The simulations showed that the determined detector background meets the scientific requirements for the Large Area Detector and is below the requested value. In order to find possibilities for minimizing the detector background, first investigations of the response of the detector background to changes in the detector geometry have been initiated.

The simulation studies of a nano-satellite of the planned HERMES mission include the predictions of the expected detector background and an observation of a gamma-ray burst to determine how strong the detector background is compared to an observed source and to estimate the expectable outcome of an observation. Since many nano-satellites on low-Earth orbits with different inclinations are planned for the HERMES mission, the simulations were performed for one low and one high inclination orbit. The constellation of nano-satellites will enable the detection and localization of transient high-energy events such as gamma-ray bursts. The first nano-satellites of the HERMES mission will be launched in mid-2020 to verify the functionality of the technology.

Contents

1 Introduction **7**

2 Geant4 Simulation Toolkit **9**

2.1 Monte Carlo Simulations 9
2.2 Structure of Geant4 Simulations 10
2.2.1 User Actions 12
2.3 Creating a Simulation Environment for in-orbit Detector Background Simulations 14
2.3.1 Isotropic Background Radiation 14
2.3.2 Normalization 16
2.3.3 Implementation of Physics Processes 19
2.3.4 Detector Quantum Efficiency 20
2.3.5 Amount of Detected Energy 21
2.3.6 Fluorescence 23

3 eXTP Simulation Studies **25**

3.1 The eXTP Mission 25
3.1.1 Mission Profile 25
3.1.2 Science with eXTP 27
3.1.3 Scientific Instruments 30
3.2 Simulated LAD Geometry 35
3.2.1 Studies of Possible Collimator Geometries 36
3.3 Primary Particle Generation 39
3.3.1 Models for GCR Particle Fluxes 40
3.3.2 Magnetic Shielding Models 40
3.3.3 Input Spectra for the eXTP Background Simulation Studies . 41
3.4 Background Spectra 42
3.4.1 Implementation of the Limited Energy Resolution 42
3.4.2 CXB Induced Background Spectrum 43
3.4.3 GCR Induced Background Spectrum 45
3.4.4 Total Background Spectrum 46
3.4.5 Background Spectrum and Detector Thickness 50
3.5 Conclusion 51

4 HERMES Simulation Studies **53**

4.1 The HERMES Mission 53
4.1.1 Mission Concept 53
4.1.2 Science with HERMES 54
4.1.3 HERMES Scientific Payload 56

4.2 Simulated HERMES Geometry 57
4.3 Primary Particle Generation 60
4.3.1 Input Spectra for Background Simulation Studies 60
4.3.2 GRB Input Spectrum for Source Simulation Studies 61
4.4 Results of the Simulation Studies 62
4.4.1 Implementation of the Energy Resolution 62
4.4.2 CXB Induced Detector Background 63
4.4.3 GCR Induced Detector Background 65
4.4.4 Total Detector Background 67
4.4.5 Results of the Gamma-Ray Burst Observation 68
4.5 Conclusion 72

5 Conclusions **75**

Chapter 1

Introduction

A challenge within the observation of most astrophysical X-ray sources is the detection of these usually rather weak sources in the presence of a strong background. Therefore, minimizing this background is an important part of planning and operating an X-ray observatory. A low background allows to reduce the observation time and to observe weaker sources, which enhances and expands the scientific output.

Since the Earth's atmosphere absorbs most of the cosmic X-rays, astronomy in this energy range began only when observations above the bulk of the atmosphere were possible. Balloons, rockets and satellites are used to carry the detectors to heights where the absorption of the X-rays is minimal. The planned observatories studied within this work will both be located on satellites in orbit around the Earth. Therefore, their detector background, i.e. detected events that are not coming from the observed source, consists of various components that differ in origin and cause:

- **Cosmic X-ray Background (CXB)**
  This nearly isotropic and diffuse sky background of cosmic X-rays is composed of different types of unresolved extragalactic sources such as active galactic nuclei (Gruber et al. 1999; Gilli et al. 2007). Photons coming from the CXB cause a measured detector background in two different ways. Photons of the high energy part of the CXB interact with the material surrounding the detector and produce secondary particles with lower energy, which can then be measured by the detector. The low energetic part of the CXB can be detected directly when the photons are coming from the field of view of the detector. These photons cannot be distinguished from the observed source photons that also come from the direction of the field of view.

- **High Energy Particles**
  These particles contribute to the detector background after interacting with the satellite and creating a high number of secondaries that then are detected. These high energy particles include solar particles and the Galactic Cosmic Rays (GCR) consisting primarily of protons. These particles can reach the satellite directly or else they are captured in the Earth's magnetic field and when the satellite crosses these regions of captured particles they contribute to the detector background. Therefore, the impact of these high energy particles depends on factors like the satellite's orbit and on the solar cycle, which affects the amount of shielding by the Sun's magnetic field.

- **Detector and Readout Noise**
  Noise (spurious events) produced by the detector and its readout electronics.

The detector background has a strong impact on the achievable sensitivity of the instrument. A quantity representing this sensitivity is the minimal flux F_{min} of a source that can still be detected by the instrument. This flux depends on detector properties such as the quantum efficiency $\epsilon(E)$ and the effective area $A_{eff}(E)$, on parameters like the measurement time T and the background flux B in the detector. It can be calculated by the following formula adapted from Fraser (1989):

$$F_{min} = n_\sigma \cdot \frac{\sqrt{B \cdot A_{det}}}{\epsilon \cdot \eta \cdot A_{eff}\sqrt{T \cdot \Delta E}} \tag{1.1}$$

with the desired statistical significance n_σ of a detection and the area of the detector A_{det} in which the fraction η of the source photons arrives. Sources with a flux below this limiting minimum detectable flux will therefore not be detected or cannot be observed by the instrument. To achieve higher sensitivity, which can lead to new discoveries, continuing efforts to minimize the detector background are made.

Since the noise caused by the detector and readout electronics can be measured in laboratories on Earth, the simulation studies in this work consider only the high energy photons and particles the detector is exposed to in space. Therefore, the impact of the photons coming from the CXB and the protons of the GCR are typically investigated using Monte Carlo simulations to estimate and optimize the detector background that will be measured by future observatories.

This thesis is structured as follows. Chapter 2 will introduce Monte Carlo simulations and the simulation toolkit Geant4 that is used. Furthermore, this chapter explains the creation of a simulation environment for in-orbit detector background simulations, which includes the implementations of simulation requirements, such as an isotropic radiation environment, and validation tests.

This work contains simulation studies for two future X-ray observatories. The studies for eXTP focus on the Large Area Detector (LAD), which is one of four scientific instruments of eXTP. Chapter 3 introduces the mission and explains how the detector geometry and the particle sources (CXB and GCR) are implemented in the simulation. The results of the simulation studies are presented and discussed later in this chapter.

Chapter 4 introduces the HERMES mission and presents the geometry and the incoming particle and photon spectra used for the simulation studies. A particular feature of the HERMES studies is the simulation of a gamma-ray burst (GRB) observation, which are the main sources that will be observed by HERMES.

The thesis will conclude with a combination of conclusions and outlooks of the simulation studies for both investigated observatories in Chapter 5.

Chapter 2

Geant4 Simulation Toolkit

Geant4 (GEometry ANd Tracking) is a comprehensive toolkit based on Monte-Carlo simulations for tracking particles through matter and electromagnetic fields. Therefore, it is applied in high energy, nuclear and accelerator physics, and it is used in studies of medical and space science. As the successor of the Geant series of software toolkits, which were developed by CERN, it is continually enhanced by the international Geant4 Collaboration. The software package, using object-oriented programming written in C++, is freely available on the Geant4 website[1] where guides and examples are also provided.

This chapter first introduces Monte Carlo simulations in general. Then the structure and components of a Geant4 simulation, as used in this work, will be described in more detail and the setup of a simulation environment will be explained. The information about Geant4 in this chapter is taken from the Geant4 website and an overview paper of Agostinelli et al. (2002).

2.1 Monte Carlo Simulations

Monte Carlo simulations use random numbers to obtain results of complex systems that range from weather forecasts to galaxy modeling. Problems that cannot be solved analytically or experiments that would be too expensive or not practicable can be solved by Monte Carlo Simulations. The information given in this Section is based on Harrison (2010).

The first versions of Monte Carlo methods were invented by the French scientist Georges-Louis Leclerc, Comte de Buffon (1707-1788). His most famous problem is known as "Buffon's needle" where the value of π is estimated by throwing needles randomly on a striped floor. Simulations based on random methods to solve previously understood deterministic problems were used by other scientists in the following centuries. But the beginning of modern Monte Carlo Simulations, which treat deterministic problems by first finding a probabilistic analogue, was during World War II. John von Neumann and Stanislaw Ulam used the method to study neutrons traveling through radiation shielding for the Manhattan Project and named it after the Monte Carlo Casino.

[1]https://geant4.web.cern.ch/

Table 2.1: Probability distribution of the dot sum when rolling two dice

sum of both dice	2	3	4	5	6	7	8	9	10	11	12
probability	$\frac{1}{16}$	$\frac{2}{16}$	$\frac{3}{16}$	$\frac{4}{16}$	$\frac{5}{16}$	$\frac{6}{16}$	$\frac{5}{16}$	$\frac{4}{16}$	$\frac{3}{16}$	$\frac{2}{16}$	$\frac{1}{16}$

The simulations are based on random numbers or computer generated pseudo-random numbers and on probability density functions (PDFs), which describes the system that is simulated. A PDF defines the range of possibilities and the relative probability for a given step in the simulation. It is normalized, which means an integration over its whole range is equal to one. A Monte Carlo simulation is based on large numbers of repetitions of individual random runs specified by the PDFs. The sum of these runs gives an impression of the behavior of the whole system. Increasing the number of runs allows the accuracy of the simulation results to improve. How good the simulation reaches reality depends also on the definition of the model, which represents the simulated system and is described by the PDFs. Therefore, the properties of the model, which are important for the searched results, should be considered by simulation and at the same time the complexity should be kept as low as possible to reduce the computing time of the simulations.

To demonstrate the basic principle of Monte Carlo simulations, a simple example is to consider two dice that are rolled many times. Rolling a single die can lead to six possible outcomes (1, 2, 3, 4, 5, 6), which occur with the same probability $\left(\frac{1}{6}\right)$. Thus, a die has a uniform probability density. This means, when only one dice is rolled many times, the resulting distribution will also be uniform with small deviations. The more runs that are made, the more uniform this distribution will be. But what happens to the resulting probability density when two dice are rolled and the sum of dots of both dice is considered? Due to the simplicity of this experiment, the resulting probability distribution can be calculated. However, it is also possible to determine it by rolling both dices many times and recording the results. Table 2.1 contains the theoretical values of the probability distribution. Figure 2.1 shows the comparison between the theoretical probability distribution (left) and the result of rolling the dice 2000 times in a simulation (right). The resulting histogram of the simulation shows the total number of incidents. To compare it with the theory, the values must be normalized by dividing them by the number of repetitions (2000). The normalization of the simulation result is an important part of Mont Carlo simulations that will be also be carried out later in this work. Comparing the shape of both distributions shows a clear similarity. More repetitions would improve this similarity even more.

2.2 Structure of Geant4 Simulations

The Geant4 toolkit provides every aspect needed for a simulation of particles passing and interacting with matter and electromagnetic fields:

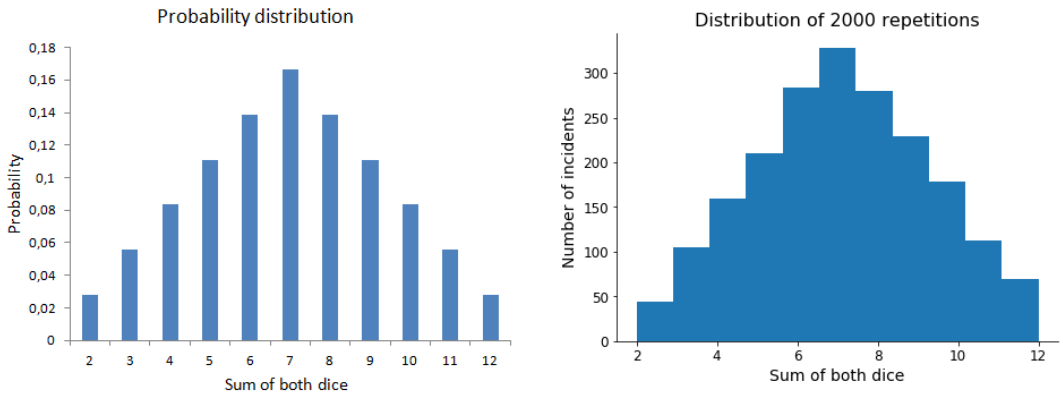

Figure 2.1: Distribution of possible dot sums when rolling two dice. (left) The theoretical values in form of the probability distribution. (right) Distribution due to simulating rolling the dice 2000 times.

- Definition of the detector and experiment design (geometry and materials)
- Generation of primary particles (particle type, energy, source structure and position, radiation pattern)
- Selection of physics processes to be considered
- Definition of sensitive detector components
- Generation of event data (simulated detector properties)
- Storage of relevant data
- Visualization of the geometry and the particle trajectories

Furthermore, a Geant4-simulation is structured hierarchically. On top there is the *run* that includes the collections of all generated particles (*events*) that share a common particle source and detector implementation. An *event* contains the generation and tracking of one primary particle and its secondary particles produced by interactions with matter or fields. When the primary and the secondary particles have lost their whole kinetic energy or left the world volume, the *event* is finished. Then the next *event* can be started, which means the primary particles are simulated one after another. Therefore, there is only a time course within a single *event*, which is reset to zero when the *event* is completed. There is no temporal relationship between the simulated particles, because each particle starts at a temporal zero point. However, since the time represented by the simulation is of particular interest, especially for normalization, it must be determined in a different way. Due to the relation between the number of simulated particles, the particle flux and the time, it is possible to calculate the simulated time, as an example in chapter 2.3.2 shows. During the *event* a *hit* is created when a particle interacts with a sensitive detector. A *hit* contains the corresponding information of the interaction. After each *event* the data is deleted. Therefore, it is the user's responsibility to save the relevant data.

2.2.1 User Actions

The categories mentioned above can be edited by the user in different classes. There are three classes which have no default behavior defined by Geant4. Hence, it is mandatory that the user programs them according to the simulation requirements. Five further classes can be optionally edited by the user to gain control of the simulation and to get more information.

Mandatory User Classes

The mandatory user classes include the detector construction, the physics list to specify the physics processes that will be used, and the definition of how the primary particles will be generated.

The whole geometry of the experiment, which includes the corresponding materials as well as the sensitive detector elements, is defined in the *user detector construction.*
The geometry is built from different volumes which are organized hierarchically. First, a world volume must be created and that must include the whole experiment geometry and therefore all further volumes. Creating a volume starts with a solid. There are many solids of the Constructed Solid Geometry (CSG) provided by Geant4 that can be used, for example boxes (G4Box), cylindrical sections or tubes (G4Tubs) and spheres or a spherical shell sections (G4Sphere). More complex bodies can be created by Boolean operations (union, subtraction, intersection) of existing solids. It is also possible to import and convert geometrical shapes from CAD systems. In the next step, physical characteristics, for example the material or sensitive detector properties are added to the geometrical characteristics and define a logical volume. When the volume (daughter volume) gets its position information and is placed in an already existing volume (mother volume), it is called a physical volume. The coordinate system, in which the position is defined, always relates to the mother volume. The only exception is the world volume because it contains all other volumes and has no mother volume.
There are several ways to define the materials for the logical volumes. Geant4 provides a data base that contains many standard materials such as oxygen, silicon or water. If materials with special properties are needed there are several possibilities. Geant4 has the G4Element class to describe any element for example by defining its atomic number, number of nucleons or atomic mass. The G4Material class can be used to describe materials with macroscopic quantities such as density, state and temperature. With this, class molecules can be built from single components, and mixtures can be defined using the mass fraction of the components.

The *user physics list* contains the physics processes and particles that are required in the simulation. Due to the huge range of processes, it is not possible to have a default physics list for all simulations in an energy range from eV to TeV. Therefore, it is the user's responsibility to choose all the relevant physics and define them in the user physics list. There are the following major physics process categories:

- electromagnetic,
- hadronic,

- decay,
- optical,
- transportation,
- parameterization and
- photolepton-hadron processes

Most of these categories have sub-categories that contain many specific processes that, for example, may depend on the particle types or energy ranges. Geant4 provides several pre-fabricated physics lists that can be used directly or modified and therefore facilitates the creation of the customized physics list. Section 2.3.3 gives examples of the user physics list, used in this work.
The particle movement in Geant4 is divided into single successive *steps*. In the beginning of every *step* a process from the physics list is chosen to be executed. The process choice depends on the smallest proposed step length. This step length is calculated for every possible process and depends on its cross-section information and on geometrical properties. Since the determination of the step length depends on the material, a *step* ends on material boundaries and a new *step* will be created. At the end of the *step* the details of the particle's interaction are implemented by the DoIt-method, meaning that changes of the particle's energy, momentum and position are updated, and secondary particles may be created. The simulation of a (primary) particle is completed when it leaves the world volume in a *step* or it is killed by the creation of secondary particles or when the particle's energy or its proposed step length is below a specified threshold (cut value). After this, the next (secondary) particle is simulated. This means that only the interaction of one particle with the detector is simulated and not the interactions with other particles. The previous mentioned cut values are set to reach a better performance by limiting the number of produced secondaries. In order not to lose any relevant particles, the limit of secondary production is linked to the particle energy or step length. For example, the step length threshold suppresses the production of secondaries whose proposed step length would not reach the threshold. In this case the remaining energy is deposited additionally in the last *step*. But since the step length depends on the material, this does not define a limit considering the particle energy. Therefore, the energy threshold must be defined additionally to avoid a production of very low energetic particles, which are not relevant for the simulation result.

In the *user action initialization* all user action classes must be defined through the SetUserAction() method. One mandatory user action class is the *user primary generator action*, which contains all information about the generation of the primary events. There are three types of primary generators provided, which are suitable for different requirements.
The G4ParticleGun offers several basic methods to define the generated particle's properties such as its energy, momentum direction and position and the number of simulated particles during the *run* can be set.
An advanced primary generator, which can be used to create more sophisticated systems, is the G4GeneralParticleSource (GPS). The GPS offers a wide range of options to define the particle source. It includes the settings of the G4ParticleGun

and allows many other ways of configuration such as particles generated on surfaces, definition of the angular distribution or particle energies defined by a spectrum. As these settings are important for the simulations in this work, the GPS was used to generate the primary particles. The GPS can be controlled by a macro-file that allows quick changes of the primary generation without changing the code and compiling again. It allows to define the particle type, the energy distribution type which ranges from mono-energetic to user defined histograms and the particle source position and structure that includes for example its shape, the angular distribution and direction.
The third possibility of generating particles is the G4HEPEvtInterface, which provides interfaces to external event generators.

Optional User Classes

These classes can be modified by the user to extend the default behavior of Geant4 and to get more control of the simulation at various stages. The *user run action* can be used for actions at the beginning and end of a *run*, while the *user event action* is responsible for the actions at the start and end of an *event*. For an individual access to the track stacks there is the *user stacking action* and to modify actions at the start and the completion of every track the *user tracking action* can be used. The fifth class is the *user stepping action* that allows to customize the behavior at every *step*.
Three of these classes were modified for the simulations of this work. The *user run action*, which manages the creation of the output file. Then the *user event action* defines which parameters are written in the output file at the end of every *event* and it calls functions which are defined in the *user stepping action* to get more information about the *steps*, for example position information.

2.3 Creating a Simulation Environment for in-orbit Detector Background Simulations

Before the actual detector simulation studies are made, a simulation environment must be set. This should include all necessary requirements to simulate a detector in space e.g. isotropic background radiation or relevant physics processes. This section is about the implementation and the validation of these requirements.

2.3.1 Isotropic Background Radiation

The aim is to simulate the detector in its future working environment in space, exposed to the radiation environment. Since the radiation arrives from all directions, an isotropic radiation environment is needed, which means a flux whose intensity is independent of direction.

Therefore, particles are generated on a spherical surface around the detector. The radiation direction is limited by an angle θ_{max} to reduce the computing time. This angle is determined by the size of the detector construction. It should form a sphere of an isotropic radiation environment which includes the whole detector geometry as shown in Figure 2.2.

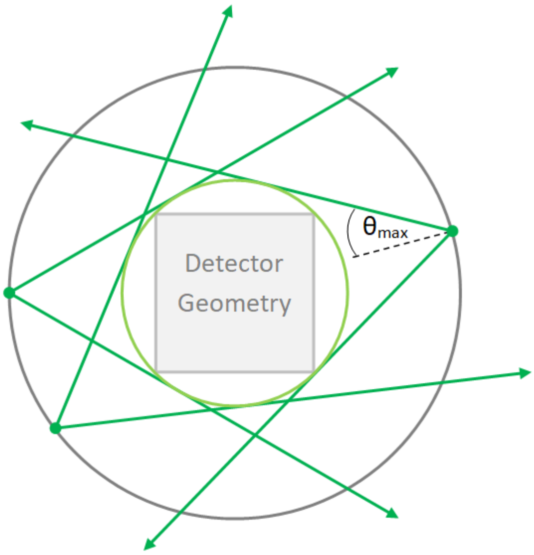

Figure 2.2: The angle θ_{max} limits the radiation direction on every beam (green) that is radiated on the surface of the outer sphere. This leads to a smaller virtual sphere (light green) where the whole detector geometry should be included to have an isotropic radiation environment.

But the spherical particle source alone does not lead to an isotropic radiation environment. Therefore, the angular distribution of the emitted primary particles can be changed as a further adjustment. An isotropic angular distribution would not lead to an isotropic flux around the detector, which can be explained by Figure 2.3. When the angular distribution is isotropic, every point of the radiating surface emits rays of the same intensity I in every direction. As the photon flux Φ is a radiation density, it increases when the area that is crossed by the rays becomes smaller. Figure 2.3 shows the two cases with different radiation angles. One is radiation that is emitted perpendicular and the second is emitted at an angle θ. It can be seen how the area perpendicular to the rays gets smaller for an observation angle $\theta > 0°$ ($A_1 > A_2 = A_1 \cdot \cos(\theta)$). Therefore, the emitting surface gets brighter when the observation angle deviates more from the perpendicular direction. To counteract this effect and to achieve an isotropic radiation environment where the flux is independent from the emission angle θ the angular distribution has to follow Lambert's cosine law. This law scales the intensity with the factor $\cos(\theta)$:

$$I(\theta) = I_{max} \cdot \cos(\theta) \tag{2.1}$$

where I_{max} is the intensity emitted perpendicular to the radiating surface and θ is the angle between the surface normal and the observation angle. Thus, the intensity and the crossed area change equally, and the photon flux is independent of the angle θ.

In summary, the particles have to be generated on a spherical surface with a cosine-law angular distribution to create an isotropic radiation environment. These requirements can be both implemented in the General Particle Source (GPS).

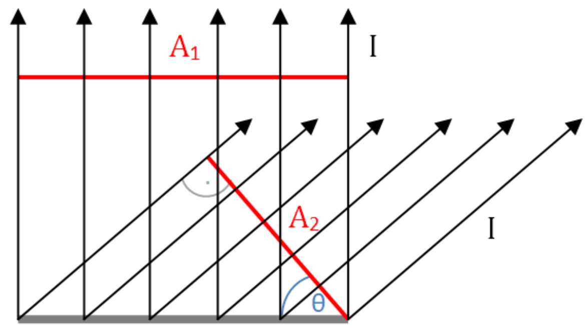

Figure 2.3: Radiating surface for an isotropic angular distribution with changing emission angle from 0° to θ. The intensity I is constant but the area that is crossed by the rays changes from A_1 to A_2 by a factor of ß$\cos(\theta)$ ($A_2 = A_1 \cdot \cos(\theta)$). Therefore, the radiation density increases and the surface shines brighter for angles $\theta > 0°$.

The illustration of creating an isotropic background radiation is demonstrated here in the example of the Cosmic X-ray Background (CXB). First, an input spectrum is needed that can be implemented in the GPS. For the CXB there is an analytic expression, which results from the fitting of High Energy Astronomical Observatory 1 (HEAO-1) and Compton Gamma Ray Observatory (CRGO) data presented by Gruber et al. (1999)). The spectrum is divided in two parts depending on the energy E:

$$\begin{aligned} 3 - 60\,\mathrm{keV}: &\ 7.877 E^{-0.29} \mathrm{e}^{-\frac{E}{41.13}} \quad \frac{\mathrm{keV}}{\mathrm{keV\,cm^2\,s\,sr}} \\ > 60\,\mathrm{keV}: &\ 0.0259 \left(\frac{E}{60}\right)^{-5.5} \\ &+ 0.504 \left(\frac{E}{60}\right)^{-1.58} \quad \frac{\mathrm{keV}}{\mathrm{keV\,cm^2\,s\,sr}} \\ &+ 0.0288 \left(\frac{E}{60}\right)^{-1.05} \end{aligned} \tag{2.2}$$

Figure 2.4 shows the CXB spectrum resulting from this formula. For the simulation this spectrum is extrapolated down to 1 keV and the expression is divided by E to get the intensity in units of photons $\times$ (keV cm^2 s sr)$^{-1}$.

In order to implement the spectrum in the energy range from 1 keV to 10 MeV in the GPS macro file, a histogram must first be extracted from the analytical expression. For this a suitable energy binning is necessary. Since it is easier to display the spectrum logarithmically, it makes sense to use a logarithmic binning to cover the energy range in an efficient way.

2.3.2 Normalization

Normalization is a key principle for obtaining meaningful results from Monte Carlo background simulation studies. The results of the simulations contain absolute values depending on the number of *events* (simulated primary particles). When making

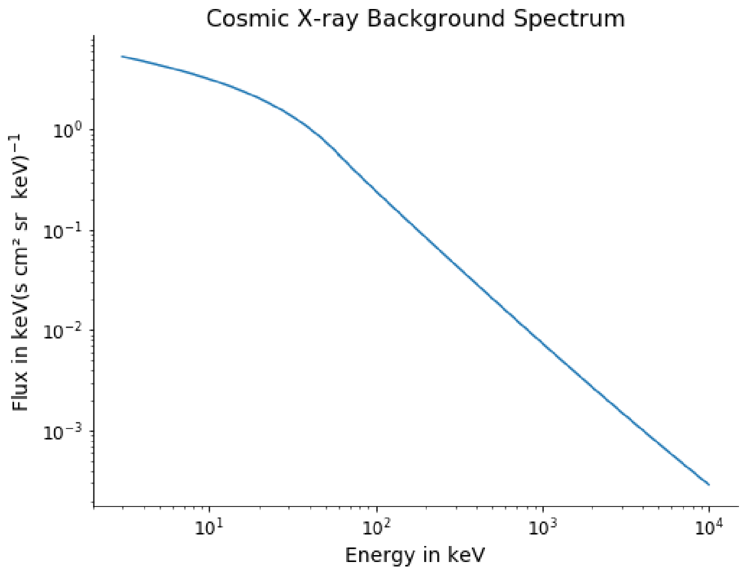

Figure 2.4: CXB spectrum resulting from Equation 2.2 based on Gruber et al. (1999). To use this spectrum as the input spectrum of the CXB photons for the simulations, it was extrapolated down to 1 keV and divided by the energy E.

a statement about the behavior in the real world the results have to be normalized. The idea is that there is a relation between the number of *events* N_S and the simulated observation time t. With this time and the geometric properties, the simulation results can be normalized.

This section will give an example of determining t by simulating a simple detector geometry that is exposed to the CXB by using the spectrum introduced in Section 2.3.1 above.
The total flux Φ, expressed as the number of photons per second, square centimeters, and steradian, is an important quantity, which can be derived from the spectrum. For this purpose, the created histogram for the GPS is integrated over the energy range of 1-10000 keV. This results in a total photon flux of $\Phi = 15.708$ photons cm^{-2} s^{-1} sr^{-1}.
With N_S and the number of particles per second n_Φ that have to be produced on the spherical particle source to create the required CXB flux Φ, the simulated observation time can be calculated:

$$t = \frac{N_S}{n_\Phi} \tag{2.3}$$

For calculating n$_\Phi$, the flux Φ has to be integrated over the sphere surface and the spatial angle considering Lambert's cosine law:

$$n_\Phi = \int\int \Phi \cos\theta \, d\Omega \, dA \tag{2.4}$$

With the spatial angle element $d\Omega = \sin\theta \, d\phi d\theta$ and the integration over the sphere's surface, which gives a factor of $4\pi R^2$, the integral can be written as

$$n_\Phi = 4\pi R^2 \int_0^{2\pi} d\phi \int_{\theta_{min}}^{\theta_{max}} \cos\theta \sin\theta \, d\theta = \Phi \, 4\pi^2 R^2 \left(\sin^2\theta_{max} - \sin^2\theta_{min}\right) \tag{2.5}$$

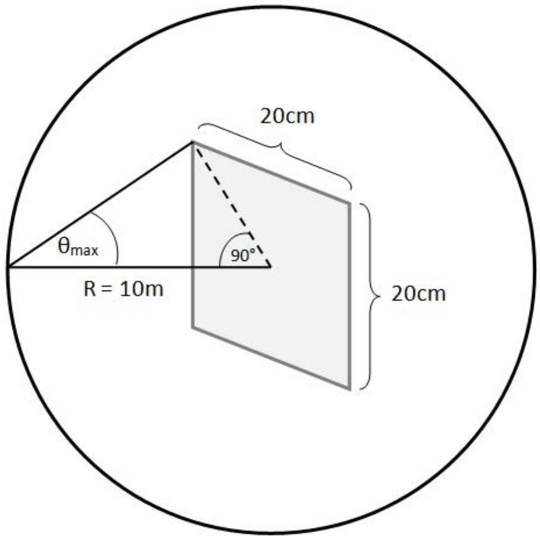

Figure 2.5: The geometry for validating the generated photon flux at the detector location. It includes the spherical particle source and a square virtual detector that counts the incoming particles. The angle θ_{max} limits the radiation direction of the primary particles so that the number of particles that would not hit the detector is kept as low as possible and at the same time the isotropy is guaranteed around the detector.

where R is the sphere radius and θ is the emission angle that can be limited by θ_{min} and θ_{max}. For the detector background simulation, the emission angle is restricted by θ_{max} only, which means $\theta_{min} = 0°$. Therefore, the simulated observation time can be calculated by

$$t = \frac{N_S}{\Phi \, 4\pi^2 R^2 \sin^2 \theta_{max}} \tag{2.6}$$

It is possible to test if the implementation of the GPS, the time calculation, and hence the normalization is done correctly. Therefore, a simple virtual detector, is used instead of the satellite geometry, which is completely transparent and counts every penetrating particle. The idea is to calculate from the count of particles the flux Φ_{det} that is generated by the simulation on the detector. If Φ_{det} agrees with the theoretical value Φ (considering statistical uncertainties), calculated from the histogram, the implementations and calculations are correct.

For this test simulation, the geometry of the GPS is the same as for the detector simulations, a sphere with 10 m radius with a limited emission angle θ_{max}, and the same CXB spectrum is used. The detector is a $20{\times}20\,\mathrm{cm}^2$ and 450 µm thick vacuum cuboid whose only function is to count the incoming particles (Figure 2.5). With these counts and the geometry, Φ_{det} can be determined as shown in the following. There is a relation between the count rate C on the detector and the radiated isotropic intensity I:

$$C = G \cdot I \tag{2.7}$$

G is the geometrical factor that depends on the detector geometry.

For a thin planar detector with an area A in an isotropic radiation environment the factor is according to Sullivan (1971):

$$G = \pi \cdot A \tag{2.8}$$

Since the particles penetrate the detector from both sides, this factor has to be doubled and therefore, the detected flux can be calculated by

$$\Phi_{det} = \frac{counts}{2\pi A \cdot t} \tag{2.9}$$

and then the two fluxes Φ and Φ_{det} can be compared and should be equivalent with statistical uncertainties.

2.3.3 Implementation of Physics Processes

The selected physics processes for the simulation studies done in this work are implemented in the user physics list (see Section 2.2.1). To create the user physics list, several predefined lists were combined. The complete implemented physics list is:

QGSP_BIC_HP_PEN

Its single components and their meanings are explained in the following.

QGSP: *QGS* stands for Quark Gluon String Model. The appendix *P* includes the G4Precompound model used for excitation.

BIC: Binary Cascade, which is reasonable for particles with energies below 5 GeV.

HP: High Precision neutron model for applications that require detailed neutron transport.

PEN: G4EmPenelopePhysics model contains "low energy" electromagnetic physics (<1 GeV). *Penelope* stands for PENetration and Energy LOss of Positrons and Electrons.

The *cut values* also mentioned in Section 2.2.1 can be set in the macro file, in which the GPS is implemented as well. These values limit the secondary particle production and can be defined as a threshold of length or energy. For the simulation studies a cut length of 1 µm and an energy threshold of 100 eV was defined. The length can be converted, depending on the particle type and material of the environment, to an energy. If this energy was to be smaller than the defined energy threshold (100 eV) then 100 eV would be used as the limit. If the energy of generated secondary particles in an interaction is less than these thresholds, they will not be produced, and the energy is instead deposited directly in the volume of the interaction.

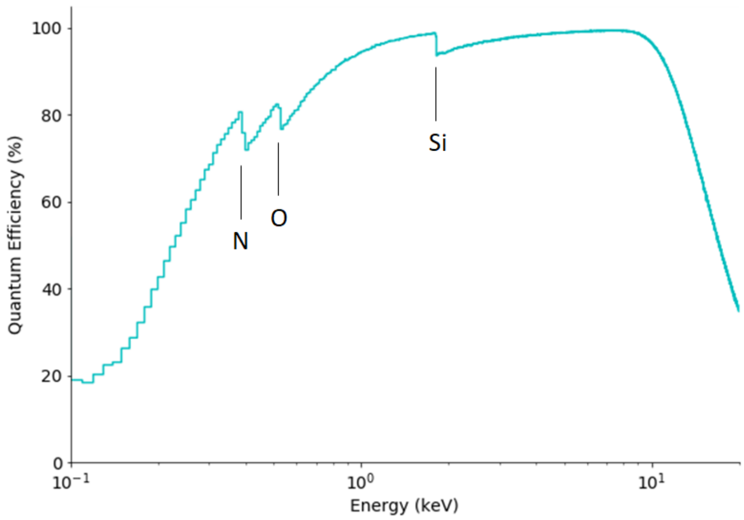

Figure 2.6: Quantum efficiency of a Silicon Drift Detector resulting from a simulation of 1 billion photons shot on the detector perpendicularly. The three rapid drops in quantum efficiency are assigned to the elements responsible for them (K-edges).

2.3.4 Detector Quantum Efficiency

Simulating the detector quantum efficiency is a quick way to see whether the geometry, including required materials and sensitive detector definition, and the physics processes are implemented correctly.

To simulate the quantum efficiency of a Silicon Drift Detector, X-rays are shot from a point source to the detector back side. The energies for the (in this case) one billion simulated photons are generated randomly, considering a flat energy distribution between 0.1 and 20 keV. The detector (20 cm × 20 cm) is made of a 450 µm thick silicon bulk, a 40 nm silicon dioxide sheet and a 40 nm silicon nitride sheet (the passivation layers of the semiconductor). But only the silicon bulk is defined as a sensitive detector, which means that interactions (deposited energy) in this volume are registered only. So if energy is deposited in one of these sheets this energy amount is not registered. During the simulation the initial energy of the photon and its deposited energy in the silicon detector is written to a CSV file.

The quantum efficiency of a detector is the probability that a photon with a certain energy will be detected. A photon is marked as detected when the complete initial photon energy is deposited in the sensitive detector volume. The ratio of the number of these detected photons and the total number of simulated photons gives the simulated quantum efficiency in Figure 2.6 with 10 eV photon energy bins (total of 1990 bins).

At lower energies, the quantum efficiency is dominated by the thin sheets. Low energetic X-rays are mostly absorbed by the silicon dioxide and silicon nitride layers and therefore are not detected in the silicon bulk. With increasing photon energy, the quantum efficiency improves. The first drop is due to the K edge of nitrogen in the silicon nitride layer and the second drop is caused by the oxygen K edge in the silicon dioxide layer. In the range of 1-10 keV the detector shows a high quantum efficiency of more than 90%, which means that nearly every photon in this energy range will be detected. Thus, the photons have enough energy to pass the layers and can interact with the detector. In this range, there is the third drop, which is caused by the silicon K edge. The slope at the high energy end depends on the detector's thickness. For the 450 µm thick silicon detector this drop starts at about 10 keV. With higher energies the photons pass the detector without interactions, which results in a decrease of the quantum efficiency.

2.3.5 Amount of Detected Energy

The quantum efficiency showed which photon energies can be detected well. Another point is the energy amount that is detected compared to the initial photon energy. To test if the sensitive detector measures the right amount of deposited energy, a mono energetic photon beam is simulated. The detector should measure every energy deposition in its volume. For example for a photon that interacts several times within the detector volume, the detector should measure the sum of the deposited energies of these interactions. When a photon interacts with the detector and leaves the detector volume afterwards with a certain kinetic energy, the measured deposited energy should be the difference between the initial and the final kinetic energy of the photon. This test was done for silicon and lead detectors with 30 keV and 50 keV beams.

Figure 2.7 shows the result of the simulation with a 50 keV beam and a 450 µm thick lead bulk that is defined as the sensitive detector. The highest counts are at 50 keV, which was expected for a 50 keV beam (Photo-peak). For the other depositions at lower energies it was checked what happened to the particle. Every particle that deposited an energy amount lower than 50 keV left the detector volume with the energy difference, or more precisely, secondary particles where created in the detector that left the detector volume afterwards.

Depending on the physics processes of the interaction, the particles deposit a different amount of energy.
Compton scattering for example leads to an energy transfer from the photon to the recoiling electron and has a limit of energy that can be deposited. This transferred energy E'_e depends on the initial photon energy E_ν as well as the scattering angle ϕ and can be calculated by

$$E'_e(\phi) = E_\nu - E'_\nu(\phi) = E_\nu \left(1 - \frac{1}{1 + \frac{E_\nu}{m_e c^2}(1 - \cos\phi)}\right) \tag{2.10}$$

with the photon energy after the interaction E'_ν, the electron mass m_e and the speed of light c. E'_e reaches its maximum for $\phi = 180°$, when the photon is scattered back directly. For an initial photon energy $E_\nu = 50\,\mathrm{keV}$ the limit of the transferred energy is $E'_e = 8.18\,\mathrm{keV}$. The histogram in Figure 2.7 suggests this limit with the drop that can be perceived around 10 keV. Better statistics could give a better resolution, but for an estimation it is enough.
Further interactions are for example Rayleigh scattering, which only changes the particle's direction, or consequences of the photoelectric effect like escape peaks and Auger electrons, where a fraction of the deposited energy leaves the detector again.

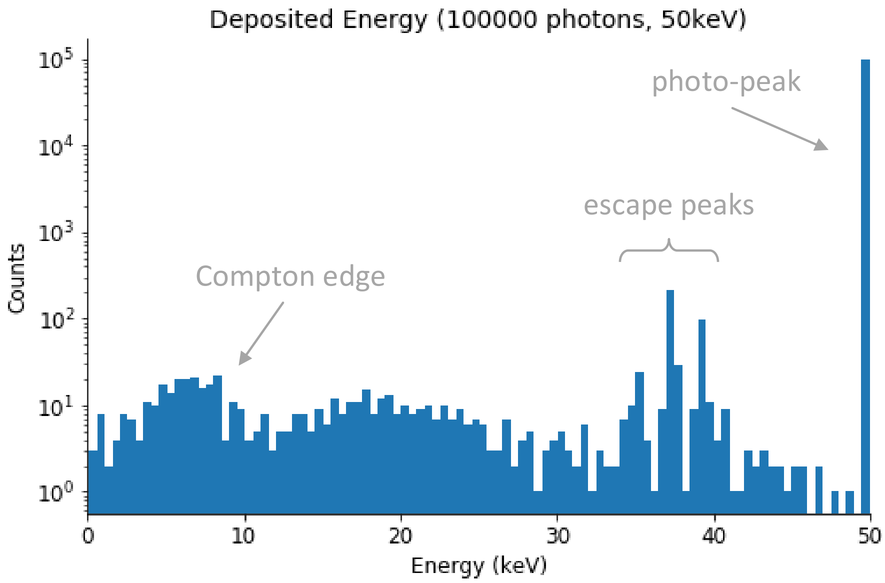

Figure 2.7: Deposited amount of energy when simulating a 50 keV mono-energetic beam of 100k photons shot on a lead bulk, which is defined as the detector. The photo-peak at 50 keV where most of the photons are detected is clearly visible and the edge caused by the Compton effect and the escape peaks caused by transitions to the L-shell of lead are recognizable.

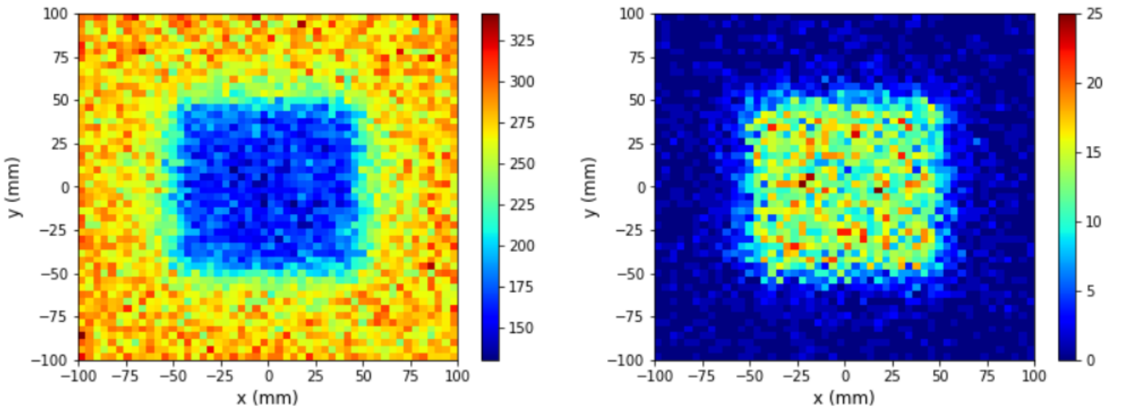

Figure 2.8: left: Image of detector hits over the whole energy range. right: 2D-histogram for hits in a narrowed energy range of 7.5-10 keV. The color scale represents the number of detected photons.

2.3.6 Fluorescence

Not only the particles that are detected directly contribute to the detector background, but also particles that first interact with materials of the satellite surrounding the detector. For example, fluorescence, which occurs when radiation excites electrons to a higher energy level, which afterwards relax to a lower level by emitting a photon. This leads to emission lines in the background depending on the materials surrounding the detector. Therefore, fluorescence should be considered by the simulation and for this reason it was checked to be implemented correctly in the simulation code.

The setup created to test fluorescence photon production consists of a $20 \times 20\,\mathrm{cm}^2$, 450 µm thick silicon detector and a $10 \times 10\,\mathrm{cm}^2$, 5 mm thick copper bulk placed 5 mm behind the detector. The particle source consists of photons emitted with 30 keV. The idea is to create a 2D-histogram of the detector hits with energies around the energy where the copper emission line is expected. Fluorescence should be seen in a bright area that has the shape of the copper bulk. To visualize the location of the detected photons, X- and Y-positions of each *event* were recorded. A 2D-histogram shows where and which number of particles interacted with the detector. For comparison, Figure 2.8 shows two images. On the left, there is the image of all the hits over the whole energy range, which shows a shadow of the copper bulk on the detector. The copper bulk shields a part of the photons so they cannot reach the detector. But when the histogram is limited to an energy range of 7.5-10 keV in which copper has three emission lines (8.05 keV, 8.03 keV, 8.91 keV), the image changes (right) and the copper shines onto the detector. This means that the fluorescence of copper becomes visible on the detector and the fluorescence is included in the simulation correctly.

Chapter 3

eXTP Simulation Studies

One of the key elements of the simulation studies in this work is the Large Area Detector background of the planned X-ray observatory eXTP. Therefore, this chapter will give an introduction to this mission and the science that will be studied by the satellite and the scientific instruments with their various features. Later the simulation will be described in more detail. The implementation of the LAD geometry for the simulation will be explained first. Then the spectra of the particles that induce the detector background are presented and discussed. The results of the simulation in the form of the background spectra, their analysis and discussion can be found at the end of this chapter.

3.1 The eXTP Mission

The enhanced X-ray Timing and Polarimetry (eXTP) mission consists of a satellite equipped with four scientific instruments. 13 Wolter-I grazing incidence X-ray telescopes form the optics of the Spectroscopic Focusing Array (SFA), which enables observations of high energy resolution (180 eV at 6 keV) and high time resolution (10 µs), and the Polarimetry Focusing Array (PFA), which allows spatial, energy and temporal resolved polarimetry. The third instrument is the Wide Field Monitor (WFM) whose cameras are able to cover about 30 percent of the sky. The Large Area Detector (LAD), which is an instrument that is simulated in this work, is characterized by its very large effective area of $3.4\,\mathrm{m}^2$ at 8 keV. Therefore, eXTP is well suited for the study of black holes, neutron stars and magnetars, which provide an insight into matter under extreme conditions as densities higher than in atomic nuclei or strong magnetic fields of $10^{14} - 10^{15}$ Gauss. Originally, there were two separate projects in 2011, the Chinese X-ray Timing and Polarimetry (XTP) mission and the European Large Observatory for X-ray Timing (LOFT) mission, which was in the selection for ESA's Cosmic Vision M3 mission. Since PLATO was selected for that project, in 2015, the LOFT and XTP concepts merged into the eXTP mission. The information presented here is mainly based on Zhang et al. (2019). Additional information about the LAD can be found in Feroci et al. (2018).

3.1.1 Mission Profile

Since the satellite's orbit influences the detector background, eXTP will be on an equatorial low earth orbit (LEO) with an altitude of 550 km and an inclination

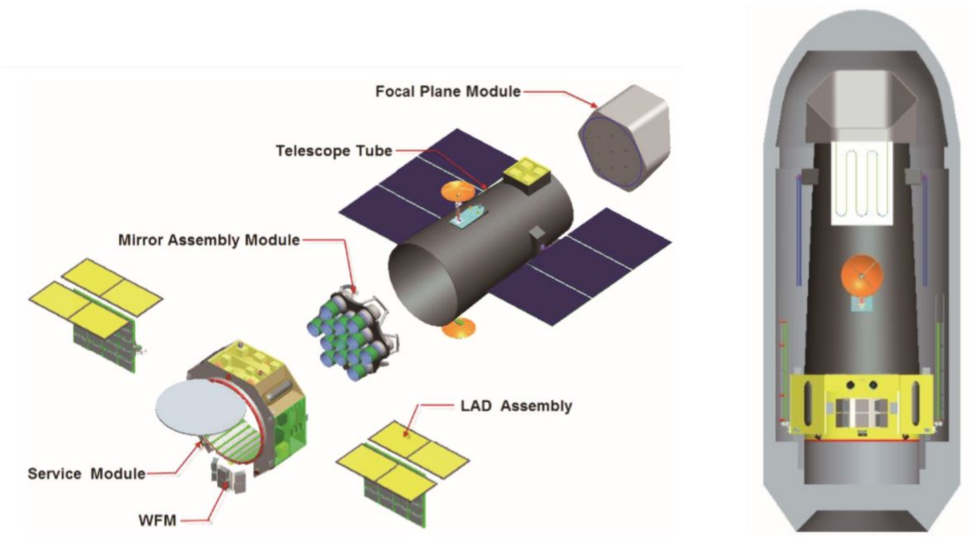

(a) Single parts of eXTP (b) Stowed position

Figure 3.1: The eXTP satellite. (a) Exploded view of the eXTP satellite with identification of its components. (b) Stowed satellite position in the launch vehicle. (Zhang et al. 2019)

of less than 2.5°. In this orbit the geomagnetic field largely shields the spacecraft against solar and cosmic particles. Furthermore, due to the low inclination the time spent in the South Atlantic Anomaly is reduced. This has a positive effect on the background because the South Atlantic Anomaly of the Earth's magnetic field is a region over the South Atlantic where the magnetic field reaches down to lower orbits. This means that there is a higher impact of radiation and charged particles on spacecrafts, whose trajectories cross this region. This anomaly arises since the dipole axis of the magnetic field has an inclination to the Earth's rotation axis and the center of the dipole is shifted with respect to the Earth's center (Mikaelian 2009).

It is planned to launch the satellite with a LM-7 Launch Vehicle from the Wenchang Launch Center in China in 2025. The lifetime of the mission is predicted to be 5 years with the possibility to to be extended to 8 years depending on the fuel.

The satellite's design is divided into different components shown in Figure 3.1a. These components are the Mirror Assembly Module (MAM) consisting of the 13 SFA and PFA mirror modules, the Focal Plane Module (FPM) hosting 13 focal plane cameras and sunshields, the LAD Assembly and the WFM. The telescope tube, which supports the MAM and FPM, defines the main structure of the spacecraft since it has to consider the focal length of 5.25 m. In order to maximize the focal length and effective area while considering the limited dimensions of the LM-7 Launch Vehicle the satellite has been designed to be foldable. Thus, the LAD assembly and the solar arrays will be folded up and the satellite can be stowed in the vehicle as Figure 3.1b shows. Then, the LAD Assembly will be deployed after launch in order for the LAD to point into the same direction as the Mirror Assembly Module.

3.1.2 Science with eXTP

The scientific instruments that combine studies in timing, spectroscopy and polarimetry of soft and hard X-rays will be used to fulfill eXTP's primary scientific goals:

- to determine the equation of state (EOS) of matter at extreme densities,
- to analyze dynamics of matter in the strong field gravity regime,
- to study quantum electrodynamics (QED) effects in the radiation emerging from highly magnetized stars.

These goals and further issues that can be studied with eXTP are described in more detail below. The information is based on Watts et al. (2019), De Rosa et al. (2019) and Santangelo et al. (2019).

Dense Matter

The objects of interest in the study of dense matter are neutron stars (NSs). In their cores the material is compressed by gravity to extreme densities (about ten times the normal density of atomic nuclei). Therefore, NSs gives an insight into matter behavior at densities that cannot be produced in laboratories on Earth. The EOS of a NS, which describes its pressure depending on the density, is related to the mass-radius (M-R) relation via the stellar structure equations. Determining the EOS of NSs allows the understanding of the microphysics inside the star. Figure 3.2 shows an example of the EOS and the corresponding M-R relation with several models that represent different scenarios of particle compositions.

There are two main techniques that eXTP will use to obtain the mass and radius of NSs. One is the pulse profile modeling of pulsations created by hotspots that can develop on the rotating NS. The relativistic effects that affect the pulse profile depend on the compactness $\left(\frac{M}{R}\right)$ of the star. Uncertainties, coming from unknown factors like the geometry of the hotspot, can be minimized with eXTP's additional polarimetry capability and then the mass and the radius can be constrained. The spin measurements of rapidly spinning NSs are the second main technique. Since the limiting spin rate is a function of mass and radius, NSs with the fastest spin rates constrain the EOS. With its large effective area, eXTP is well suited to find many of the required spinning NSs.

Accretion in Strong Field Gravity

To study matter in strong field gravity, black holes provide a suitable environment. The accretion disk of super-massive black holes in active galactic nuclei (AGN) and the stellar-mass black holes in X-ray binaries that may reach the innermost stable circular orbit (ISCO), enable us to study the deep potential well generated by the black hole and to infer its mass and spin. The spin plays an important role for winds and jets of black holes, as it powers gamma ray bursts. The spin distribution helps to understand the formation and development of black holes. Observations of matter in strong field gravity can also be used to verify some of the crucial predictions of General Relativity (GR).

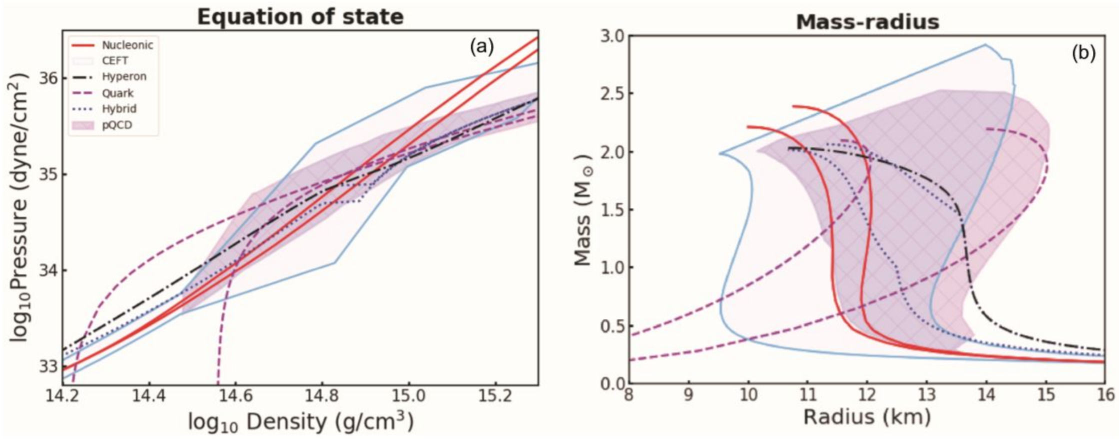

Figure 3.2: (a) Equation of state and the corresponding (b) Mass-Radius Relation for several models with different microphysics. Models: Nucleonic (neutrons, protons), Quark (u, d, s quarks), Hybrid (inner core of uds quarks, outer core of nucleonic matter), Hyperon (inner core of hyperons, outer core of nucleonic matter), CEFT: range of nucleonic EOS based on Chiral Effective Field Theory (CEFT), pQCD: range of nucleonic EOS that interpolate from CEFT at low densities and match to perturbative QCD (pQCD) calculations at higher densities. (Watts et al. 2019)

Two major direct diagnostics for matter behavior in strong field regime in black holes are the relativistically broadened iron line and the relativistic time-scale variability. The intrinsically narrow Fe Kα line is emitted in the inner accretion disk and is broadened and distorted by several effects. These include special relativistic effects, such as the Doppler effect, and relativistic aberration and GR effects, such as gravitational redshift and light bending. Analyzing this line gives information about the innermost disk radius. If the radius corresponds to the ISCO, the black hole spin can be inferred. A further possibility to measure the spin is model fitting of thermal emission coming from accretion disks around black holes in X-ray binaries. Relativistic time-scale variability, in form of quasi-periodic oscillations (QPOs), can be observed in stellar mass black holes. Modeling these low- and high-frequency QPOs enables measurements of the mass and spin of the black hole.
Furthermore, eXTP will provide measurements of the structure of the innermost regions around accreting black holes. Time resolved spectral studies and time averaged polarimetric measurements will give information about the complex environment of AGNs and in combination of SFA and LAD, measurements of the turbulence and density structure in the disk winds of X-ray binaries are enabled.

Strong Magnetic Fields

Objects like magnetars, accreting X-ray pulsars and rotation-powered pulsars provide suitable conditions to study physics in extremely strong magnetic fields. These objects are types of neutron stars, or more precisely pulsars, which are distinguished by their source of power.

Magnetars have extremely high magnetic fields ($B \approx 10^{14-15}$ G) and they are highly variable X-ray sources with changes in flux up to a factor of a thousand. These variabilities can be on different time scales, as short bursts (< 1 s) that can reach super-Eddington luminosities, intermediate flares (1-40 s) and giant flares (≈ 500 s) that can release energy of up to 10^{35} erg in < 0.5 s. Some outbursts can even last several weeks, or even years. eXTP will be able to observe and study their bursts, outbursts and timing behavior. This includes glitches, which are sudden changes of the spin frequency. There are several approaches that could explain the origin of such glitches e.g. collisions with small bodies and emission of enhanced particle winds. Searching for precession in magnetars will enable the verification of the current models of magnetars and constraining important parameters. The braking index n, which is defined as:

$$n = \frac{\nu \ddot{\nu}}{\dot{\nu}^2} \tag{3.1}$$

with the pulse frequency ν and its first and second derivative, reflects the physics of the pulsar spin-down torque. The LAD allows more effective timing measurements of magnetars in the X-ray band with its large detection area and so the braking index can be constraint for more sources.
The bright accreting X-ray pulsars are a key target for X-ray polarimetric observations. Analyzing the polarization of the emerging radiation provides information about the geometry of the emission region.
Observations of spectral properties permit the search for cyclotron lines, which are also known as the cyclotron resonance scattering features (CRSF), in the X-ray spectrum. The electron CRSF is a line-like absorption that can be found in highly magnetized accreting NS spectra. The electron movement perpendicular to the magnetic field corresponds to discrete energy levels, the Landau levels. Resonant scattering of photons, meaning that the photons have the amount of energy to lift an electron into a higher Landau level, leads to the absorption lines in the spectrum. The expected line energies E_{cyc} are:

$$E_{cyc} = \frac{n}{1+z} \frac{\hbar\, e\, B}{m_e\, c} \tag{3.2}$$

where n is representing the number of Landau levels involved, z is the gravitational redshift due to the NS mass, e is the electron charge, B is the magnetic field in the scattering region, m_e is the electron mass, and c is the speed of light (Staubert et al. 2019). Therefore, the measurement of E_{cyc} gives direct conclusions of the magnetic field in this region. Cyclotron lines of protons can be found in spectra of magnetars. The behavior is the same as for the electrons, but E_{cyc} is calculated with the proton mass instead of the electron mass. This means that the difference between the Landau levels becomes much smaller. eXTP's LAD will be able to measure spectral parameters of the CRSF less than several hundreds of seconds over a wide range of luminosities.

A further goal is the measurement of the polarization of light in strong magnetic fields that could test the first prediction of quantum electrodynamics stating that the propagation of light is affected by the magnetic field. eXTP will therefore not only observe neutron stars and magnetars that have strong magnetic fields but also e.g. black holes with weaker magnetic fields.

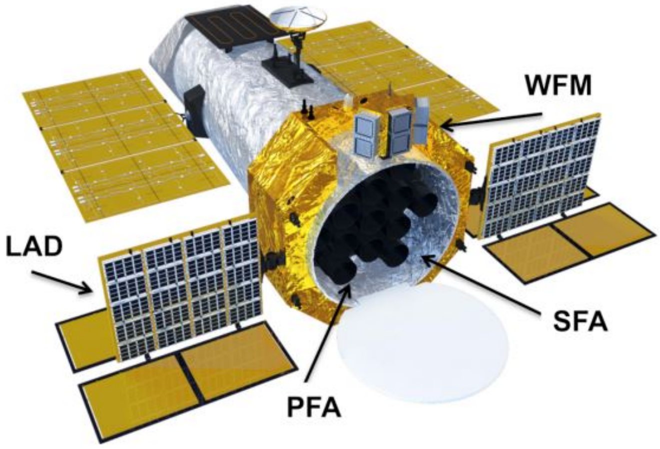

Figure 3.3: Artistic view of the current eXTP design showing the location of the instruments. (Zhang et al. 2019)

3.1.3 Scientific Instruments

This section focuses on the four scientific instruments that will make this research possible. Although the simulation studies of this work refer only to the LAD, the other instruments are also presented to complete the idea of eXTP. Figure 3.3 shows the eXTP satellite and where the Large Area Detector (LAD), the Wide Field Monitor (WFM) and the Spectroscopic and the Polarimetry Focusing Array (SFA & PFA) are located.

Spectroscopic Focusing Array

The two focusing instruments are based on grazing-angle Wolter-I telescopes with a focal length of 5.25 m and an aperture of ≤ 510 mm in diameter. These types of telescopes are made of nested mirror shells with hyper-parabolic and parabolic mirrors that use the grazing incidence angle for a total reflection of the X-rays. Each telescope is expected to have a collecting area of about $\geq 900\,\mathrm{cm}^2$ at 2 keV and $\geq 550\,\mathrm{cm}^2$ at 6 keV. The key parameters are summarized in Table 3.1.

Nine of these telescopes are optimized for spectral and timing observations in an energy range of 0.5-10 keV and form the optic module of the SFA. Together, they will provide an effective area of about $7400\,\mathrm{cm}^2$ at 2 keV. The field of view (FoV) is expected to be about 12 arcmin. The SFA will enable high-resolution observations of soft X-rays with an energy resolution of 180 eV at 6 keV and a time resolution of 10 µm. A schematic view of the components of one SFA telescope is shown in Figure 3.4. Each telescope is equipped with an array of 19 hexagonal Silicon Drift Detectors (SDDs) (Figure 3.5). The detectors have a sensitive silicon layer that is 450 µm thick and provides an excellent quantum efficiency in the required energy range. There is a filter wheel in front of the detector, which has four positions with different features, which can be used for observations, ground tests, calibration and protection.

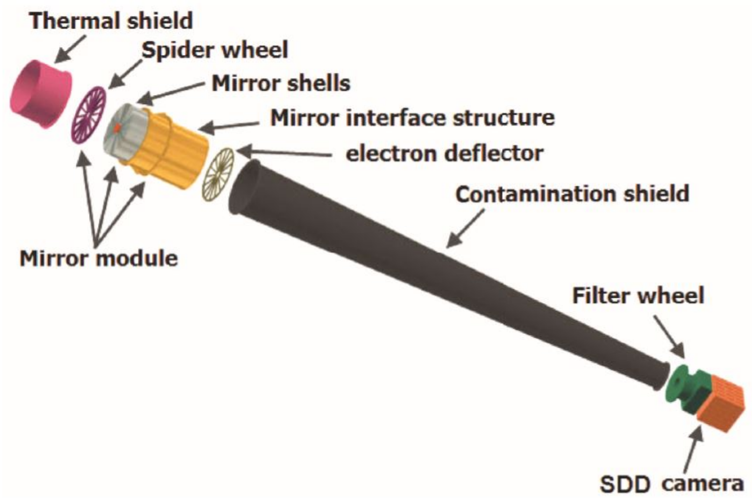

Figure 3.4: Exploded view of one SFA telescope. (Zhang et al. 2019)

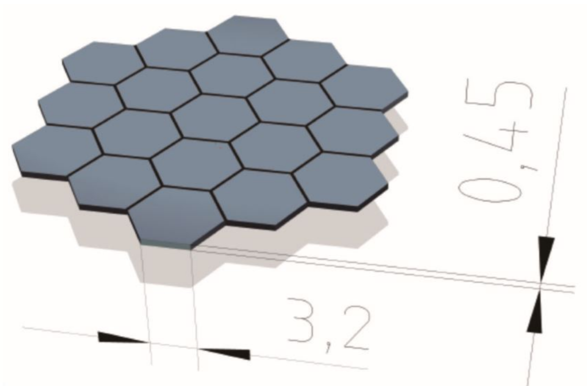

Figure 3.5: SDD array for a SFA detector with 19 hexagonal cells of 3.2 mm side length and 450 µm thickness. (Zhang et al. 2019)

Table 3.1: Main specifications of one SFA/PFA telescope.

Parameter	Value
Energy range	0.5-10 keV
Collecting area	$\geq 900\,\mathrm{cm}^2$ at 2 keV
Energy resolution (FWHM)	<300 eV at 6 keV
Field of view	≥ 12 arcmin
Angular resolution SFA	1 arcmin (HPD)
Angular resolution PFA	30 arcsec (goal 15 arcsec, HPD)

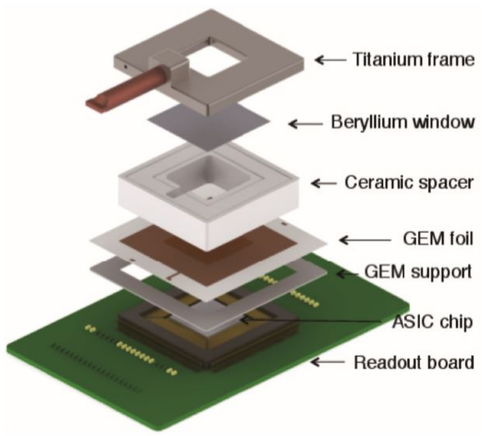

(a) Components of the GPD.

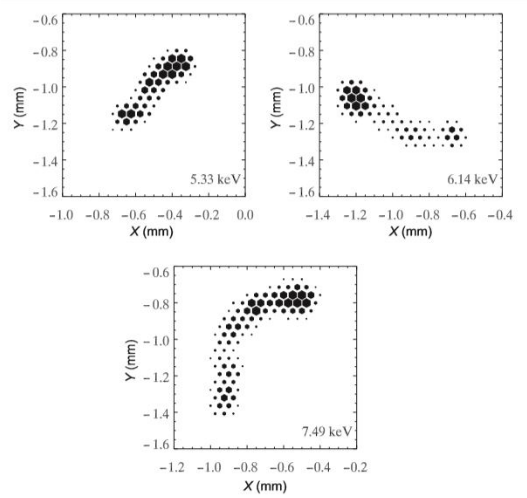

(b) Measurements of GPD

Figure 3.6: The PFA Gas Pixel Detector (GPD). (a) Exploded view of GPD and the identification of its components. (b) Examples of 2D ionization tracks at different energies. (Zhang et al. 2019)

Polarimetry Focusing Array

The PFA uses four of the Wolter-I telescopes that are optimized for X-ray imaging polarimetry in the energy range of 2-8 keV. With an angular resolution of <30 arcsec, the PFA is the only instrument of eXTP that can identify and resolve source confusions. It therefore enables high sensitive spatial, energy and temporal resolved X-ray polarimetry.
A gas pixel detector (GPD) is used as the focal plane detector for polarimetry measurements. The structure of the GPD is shown in Figure 3.6a. It consists of a gas chamber filled with dimethyl ether and sealed by a beryllium entrance window. Incident X-rays are converted into photoelectrons in this chamber. Secondary electrons, ionized by the photoelectron, are moved by a drift field of about $2\,\mathrm{kV\,cm^{-1}}$ towards the anode. A gas electron multiplier (GEM), located above the anode, multiplies the number of electrons for an adequate signal-to-noise ratio. The pixelated readout ASIC chip is placed beneath the GEM and collects and measures the charges after multiplications. The measurements are 2D ionization tracks (Figure 3.6b) of the photoelectrons that allow to reconstruct the emission angle and therefore the polarization of the incident X-ray can be inferred.

Wide Field Monitor

Three pairs of coded mask cameras with position-sensitive SDDs form the WFM that observes about 33% of the sky. Observations with the WFM can be done in an energy range of 2-50 keV with an energy resolution of about 300 keV at 6 keV. The main parameters of the WFM can be found in Table 3.2. The cameras in one pair are oriented orthogonally to each other. This allows the determination of 2D source positions by combining the images of both cameras as Figure 3.7a shows. The central camera pair is oriented along the LAD pointing axis and the two pairs beside it are rotated by $\pm 60°$ (Figure 3.7b) to cover a wide field of the sky. Each camera consists of a coded mask due to which incoming photons project a mask pattern onto

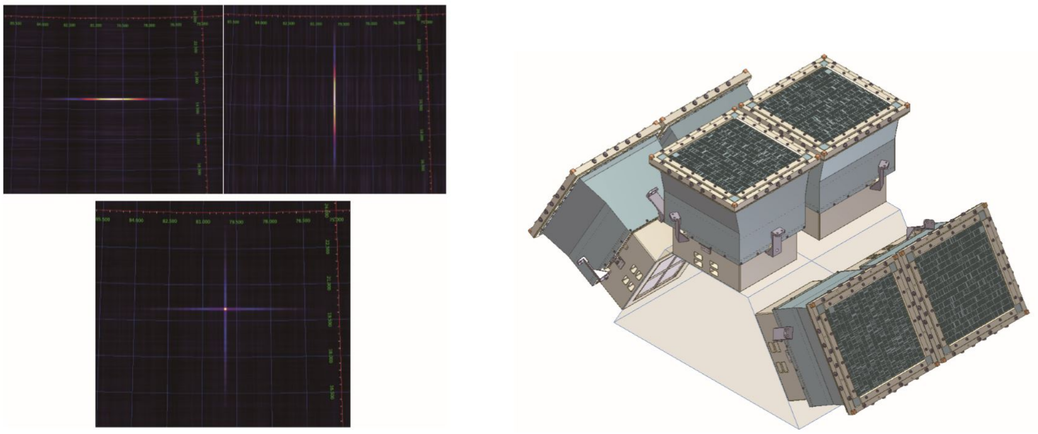

(a) WFM position measurent (b) Camera pairs of WFM

Figure 3.7: Wide Field Monitor (WMF). (a) Determining the source position by combining measurements of X- and Y- direction. (b) The three camera pairs of WFM, which are tilted by 60°. (Zhang et al. 2019)

Table 3.2: Main specifications of the WFM.

Parameter	Value
Energy range	2-50 keV
Energy resolution (FWHM)	< 300 eV at 6 keV
Field of view at 0% response	5.5 sr
Time resolution	< 10 µs for event data
	≤ 300 s for images

the SDDs that is then used to reconstruct the direction of the incoming photons. A collimator, covered by a tungsten sheet as a background shield, is placed between the mask and the detector tray, which holds four SDDs topped with a beryllium foil, to protect them against micrometeoroids and debris. The WFM with its large field of view will be very useful to detect counterparts of gravitational wave sources and it will be able to detect around 100 gamma ray bursts (GRBs) per year.

Large Area Detector

As the name suggests, the LAD provides an extremely large collecting area. Two panels with 40 modules and 640 detector-collimator units enable an effective area of 3.4 m^2 at 8 keV. Photon-by-photon observations with high resolution energy and time measurements in the energy range of 2-30 keV allows high-quality spectral-timing studies in the X-rays. The energy range can be expanded even up to 80 keV for out-of-field-of-view burst events. The key elements of the LAD are the large-area SDDs and the capillary plate collimators, which limit the FoV to 0.95° in order to reduce source confusion and the X-ray background. The low weight of these elements, which is ten times lighter than earlier designs based on traditional proportional counters and mechanical collimators, is remarkable. Table 3.3 gives an overview of the main LAD specifications.

Table 3.3: Main specifications of the LAD.

Parameter	Value
Energy range	2-30 keV (up to 80 keV)
Effective area	$3.4\,m^2$ at 8 keV
	$0.37\,m^2$ at 30 keV
Energy resolution (FWHM, at 6 keV)	<260 eV (all events)
	<200 eV (40% of events)
Field of view	<60 arcmin
Time resolution	10 µs

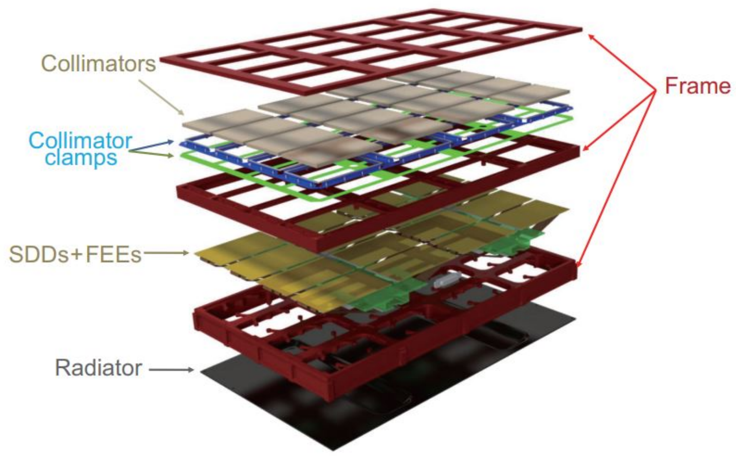

Figure 3.8: LAD module structure. (Zhang et al. 2019)

Each LAD panel holds an arrangement of 5×4 modules. The exploded view of such a module is shown in Figure 3.8. It contains 4×4 large area SDDs and 4×4 capillary plate collimators. These capillary plates (Figure 3.9) consist of a 5 mm thick sheet of lead-glass perforated by thousands of micro-pores. The open area ratio of these micro-pores is $\geq$ 75%. Between collimator and SDD is an optical-thermal filter consisting of an aluminum coated Kapton layer that guarantees transmission $>90\%$ at $\geq$ 2 keV and a 10^{-6} filtering of the IR/Visible/UV wavelengths. The filters and the capillary plates are held by the Collimator Frame. Each SDD is equipped with the Front-End Electronics (FEE) and, together with the Module Back-End Electronics, they are hosted in the Detector Frame. A 300 µm lead back-shield is placed behind the SDDs to shield the detectors from the part of the diffuse Cosmic X-ray Background which hits the detector from the back. The module's backside cover is an aluminum 2 mm thermal radiator which is used to dissipate the heat from the module. More details of the dimensions of a LAD module will be given in the next section about the LAD geometry used for the simulations.

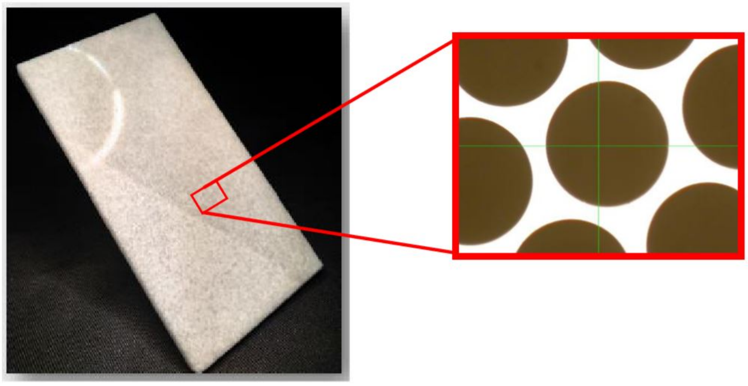

Figure 3.9: Prototype of the LAD capillary plate with a zoom of the micro pores (dark spots). (Feroci et al. 2018)

3.2 Simulated LAD Geometry

The LAD Assembly consist of two panels with 20 modules each. In this work the detector background spectrum based on the geometry of one module consisting of 16 SDDs is obtained via a Geant4 Monte Carlo simulation. The geometry of such a module (Figure 3.8) was simplified for the simulation and considers the collimator plates, optical filters, SDDs, the lead shield and the aluminum radiator surrounded by an aluminum frame.

In the following the structure of the LAD geometry, which is used for the simulations, is explained more detailed. The module is divided in 16 identical detector packages and one package includes:

- A 5 mm thick collimator simulated by a cuboid of lead glass with a reduced density of 25% to consider the 75% open area ratio of the micro pores. (Studies of finding a reasonable collimator representation for the simulations can be found in Section 3.2.1)

- An optical filter located behind the collimator. It consists of a 1 µm Kapton foil coated on both sides with 40 nm aluminum.

- The Silicon Drift Detector. It contains a silicon-dioxide and -nitride layer of 40 nm thickness each, then an 450 µm thick silicon bulk, which is defined as the sensitive detector volume, and an additional silicon-dioxide sheet of 30 nm on its backside.

- One aluminum frame that surrounds these layers.

This package is replicated 16 times and arranged in a 4×4 scheme. To complete the module, a lead shield of 300 µm and an aluminum radiator of 2 mm thickness are mounted on the backside of this arrangement and an additional aluminum frame surrounds the whole configuration. Figure 3.10 gives an impression of this construction and the dimensions.

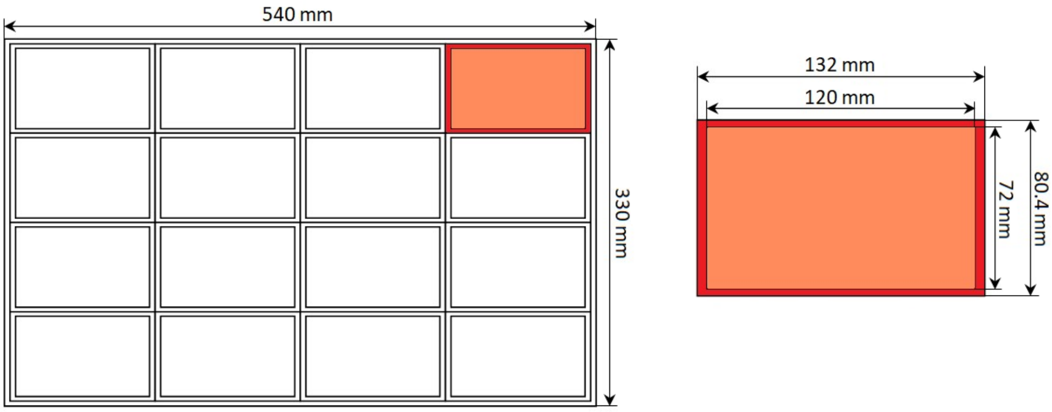

Figure 3.10: Dimensions of the LAD module used for the simulations

3.2.1 Studies of Possible Collimator Geometries

One capillary plate hosts about one million micro pores, and to simulate these pores one million tubes must be generated. Simulating 16 of these capillary plates for one LAD module would lead to a high simulation time because the high amount of generated volumes creates many simulation *steps* since a *step* ends at each volume boundary at the latest. This also requires a large memory capacity for each event. Therefore, it can be useful to define the collimator as a lead glass box with reduced density. This means, the lead glass perforated by the micro pores is replaced by a homogeneous lead glass plate, where the density of lead glass is reduced according to the open area ratio of 75% of the pores. Thus, the density is reduced to 25% of the original density. Another idea was to enlarge the pores so that less tubes have to be created. To figure out which method is more reasonable, test simulation runs were performed for both possibilities with the CXB spectrum. As a reference, a smaller detector with a size of about $20 \times 20\,\text{mm}^2$ was simulated with the correct sized micro pores of about 83 µm in diameter. Figure 3.11 shows three spectra resulting from the different geometries:

i) One LAD module with capillary plates with pores of 977.2 µm in diameter.

ii) Small test detector geometry with a capillary plate with realistic sized pores of 83.06 µm in diameter.

iii) One LAD module with collimators of reduced density.

The first thing that stands out is the high detector background in the energy range of 2 - 25 keV in case (i) compared to the other geometries. It seems that this construction leads to a disproportionately high background flux compared to spectrum (ii). This is due to the fact that the larger pores are not able to shield the background to the same extent as the actual LAD collimator does. Therefore, this geometry is not practical to achieve representative results. There are also noticeable differences between spectrum (iii) and spectrum (ii). Especially the bump at higher energies of spectrum (ii) is surprising because neither spectrum (i) nor spectrum (iii) shows this phenomenon. But also, the total flux in (ii) is higher than in (iii). To clarify if the only reason for these differences stems from the difference in sizes of geometry (ii) and (iii), a further test was made. A fourth and fifth geometry was created.

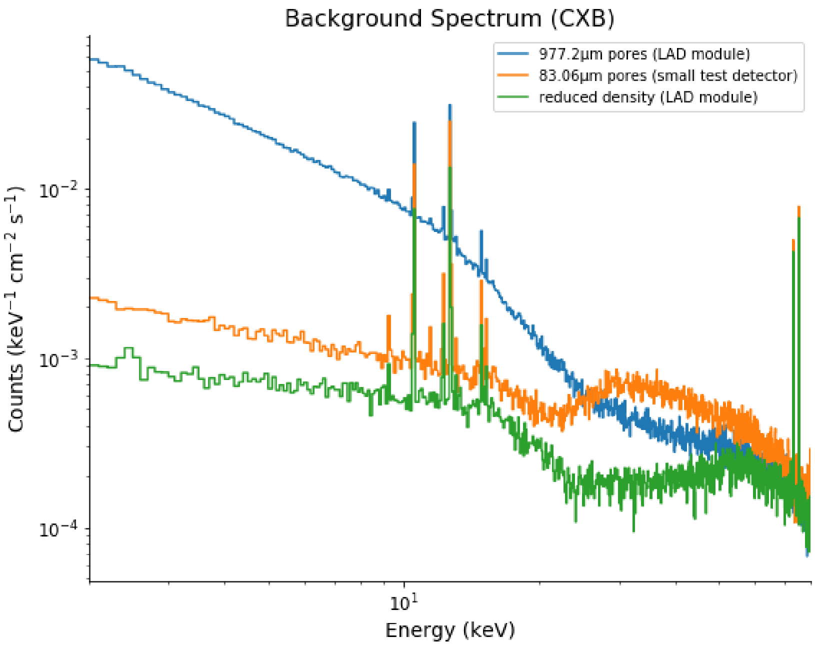

Figure 3.11: Background spectra resulting from different detector geometries. Blue: The highest detector background is measured by the geometry of one $540 \times 330\,\mathrm{mm}^2$ LAD module with capillary plates with pores of 977.2 µm in diameter (i). Orange: The small test detector geometry of $19.975 \times 19.975\,\mathrm{mm}^2$ with a capillary plate with realistic sized pores of 83.06 µm in diameter (ii) measures a lower detector flux in an energy range of 2 - 25 keV. Then the flux shows a bump at higher energies. Green: The spectrum measured by one $540 \times 330\,\mathrm{mm}^2$ LAD module where the collimators are replaced by lead glass bulks of reduced density (25% of original lead glass density) (iii) is slightly weaker than the orange spectrum and has a similar shape in the range of 2 - 25 keV. But it doesn't show the bump at higher energies.

Geometry (iv) includes one LAD module with capillary plates of 97.72 µm pores. Since the pores are simulated by tubes that are subtracted from a box with a square base area, the detector dimensions have to be integer multiples of the side length of the square to avoid overlapping volumes in the geometry. A diameter of 97.72 µm leads to a side length that meets that condition and the diameter is close to the real diameter of the micro pores. Geometry (v) also has 97.72 µm pores but has the small test detector size. Figure 3.12 shows the spectra resulting from geometry (ii), (iii), (iv) and (v). Since geometry (iv) does not lead to the bump at high energies and (v) shows the bump, it is reasonable to assume that the bump can be attributed to the reduced size of the test detector. It suggests that a simulation of the whole LAD geometry with 83.06 µm pores would lead to a similar spectrum as the spectrum resulting from geometry (iv). Therefore, it is an acceptable assumption that spectrum (iv), and hence spectrum (iii), reflects the real background spectrum of the LAD module. This means that the geometry with the reduced density collimator is a suitable choice for the simulation, considering the implementation of the collimator properties with respect to background radiation and an appropriate computing time.

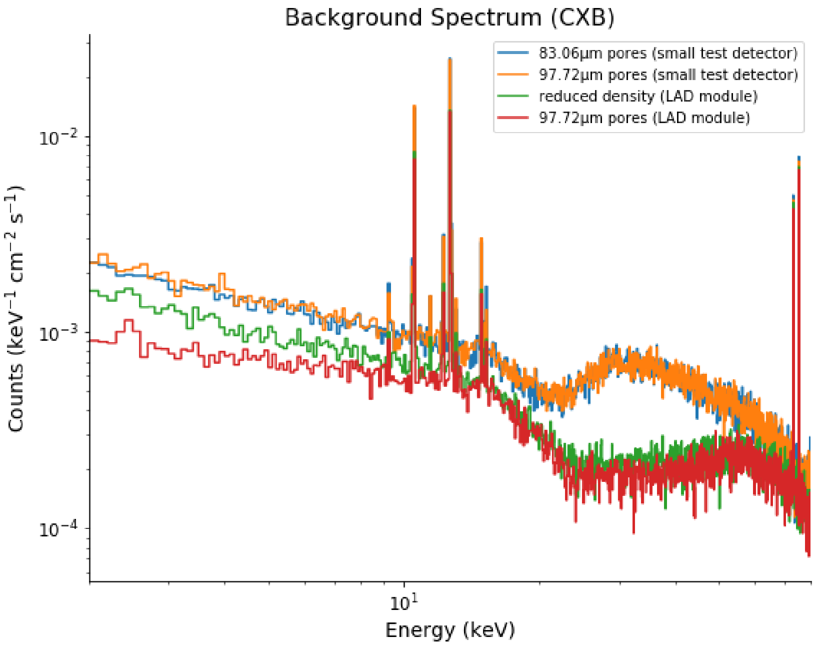

Figure 3.12: Background spectra resulting from different detector geometries for further validation. Blue: Small test detector geometry of 19.975×19.975 mm^2 with a capillary plate with realistic sized pores of 83.06 µm in diameter (ii). Orange: Small test detector geometry of 20×20 mm^2 with a capillary plate with pores of 97.72 µm in diameter (v) Green: The LAD module where the collimators are replaced by lead glass bulks of reduced density (iii). Red: A whole LAD module with capillary plates of 97.72 µm in diameter (iv). The blue and the orange spectra, which both are measured by the miniaturized detectors, are similar in shape and strength and show the bump at around 25 - 60 keV. The green and the red spectra have a similar shape but do not show the bump. The green spectrum has a slightly higher flux than the red spectrum, especially at energies < 10 keV.

3.3 Primary Particle Generation

The following particle contributions were considered in creating the radiation environment for the LAD simulations:

- photons coming from the cosmic X-ray background (CXB) and
- protons of the galactic cosmic rays (GCRs).

To generate an isotropic flux of primary particles for these simulations the approach of a sphere around the satellite with restricted emission angle (as described in 2.3.1) was done.

A representative proton spectrum of the GCRs in the appropriate orbit can be obtained with the help of ESA's Space Environment Information System[1] (SPENVIS). It is an online interface, which contains a comprehensive collection of space environment models, to create spacecraft trajectories and to determine the impact for the respective orbit. SPENVIS provides several packages that include these models and offer analyzing and simulation tools. These packages can be divided into:

- Coordinate generators,
- radiation sources and effects, e.g. cosmic rays, solar particles and particles trapped in radiation belts,
- atmosphere and ionosphere models,
- spacecraft charging to solve problem coming from spacecraft/environment interactions,
- magnetic field models,
- models for orbital debris and meteoroids ,
- miscellaneous tools that are not covered by the previous packages, and
- Geant4 tools.

The package of radiation sources and effects was important for this work. In its radiation sources category, the radiation environment in orbit created by the galactic cosmic rays can be obtained by different models that represent the GCR. But first the spacecraft's trajectory must be defined by certain orbit parameters. The parameters used for eXTP can be found in Table 3.4. In the category *Radiation sources and effects*, the GCR flux is one of the radiation sources. Various inputs are required to create the GCR spectra. First, the particle types are specified. In this case, only protons are selected. Then, the GCR model and the magnetic shielding can be chosen.

In the following two GCR models and two models for magnetic shielding, which were used in this work, are introduced briefly.

[1]https://www.spenvis.oma.be/

Table 3.4: Parameters used to create the spacecraft trajectory of eXTP in SPENVIS.

Parameter	Value
Altitude	550 km
Inclination	2.5°
Mission Duration	5 years
Orbit Start	01/01/2026

3.3.1 Models for GCR Particle Fluxes

For the galactic cosmic ionized particles that enter the solar system and can affect spacecrafts there are several models to predict the continuous and isotropic flux. Altogether there are four different models available in SPENVIS: ISO 15390, CREME96, CREME86 and the the Nymmik et al. (1996) model. The different modeling approaches taken in the individual models translate into different GCR fluxes, mostly at the lower energies as Figure 3.13 shows. The intensity of the GCR flux also changes with the activity of the Sun that follows a 22-year cycle. There is an anti-correlation between the Sun's activity and the intensity of the GCR (Ross & Chaplin 2019). When the Sun's activity reaches its maximum, its magnetic field is stronger so more charged particles of the GCR are deflected and therefore, the GCR flux is at its minimum. On the other hand, when the Sun's magnetic activity is at its minimum the GCR flux reaches its maximum.

The models considered for this work are the ISO 15390 and the CREME96 model, which allow to study the impact of these different spectra on the detector background.

ISO 15390 is the International Standard for estimating the radiation impact of galactic cosmic rays on hardware and other objects when in space. It considers variations of the flux due to the solar activity and the Sun's polar magnetic field throughout 22-year cycles.

CREME96 (Tylka et al. 1997) is based on the Nymmik et al. (1996) model and corresponds to the cosmic ray maximum situation, as observed in 1986-1987, during solar minimum. It also considers anomalous cosmic rays and it includes a low-energy component, where the model differs the most from the ISO 15390 model (see Figure 3.13).

3.3.2 Magnetic Shielding Models

Since the GCR models deliver fluxes outside the magnetosphere, they can be subsequently retrofitted with a magnetic shielding caused by the Earth's magnetic field. SPENVIS implements three methods for calculating the rigidity-cutoff[2] of the geomagnetic field. These models are called: Størmer with eccentric dipole model (Störmer 1930), Shea & Smart (1967) with the IGRF[3] model and Størmer upgrade. The first two models are used in this work to consider the cases of rather strong and weak magnetic shielding.

[2] A threshold for penetration of energetic cosmic ray particles through Earth's geomagnetic field.
[3] International Geomagnetic Reference Field

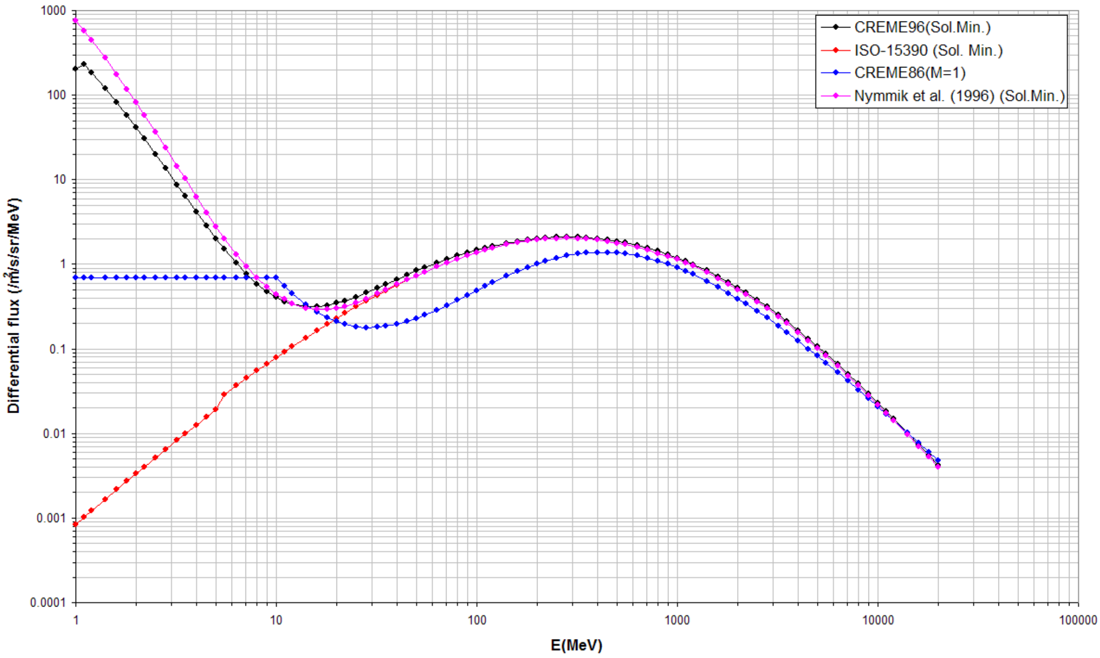

Figure 3.13: The proton GCR flux near Earth predicted by the different GCR particle flux models at solar minimum. (https://www.spenvis.oma.be/)

The difference between these methods will become clearer in the next section, which shows the spectra resulting from combining both GCR models with both magnetic shielding methods.

3.3.3 Input Spectra for the eXTP Background Simulation Studies

Since there are not only one but several GCR models available for typical low Earth orbits, the simulations are also made with different models. Then the results can be compared and the effects of the different models on the detector background become clearer. Therefore, spectra were created for the CREME96 and the ISO 15390 model once with the Størmer magnetic shielding (Figure 3.14a) and then with the Smart and Shea shielding (Figure 3.14b). The figures show that the Størmer method results in higher shielding of the GCR than the Smart and Shea method. Because the strong shielding blocks the GCR at lower energies, spectra (1) and (2) only start at about 7×10^3 keV and become similar in flux towards higher energies while the spectra created with the soft shielding, (3) and (4), differ especially towards lower energies. Therefore, several simulations with different proton spectra (1), (3), and (4) were made. Since the spectra with the Størmer shielding are quite similar, only the CREME96 (1) spectrum was simulated here.

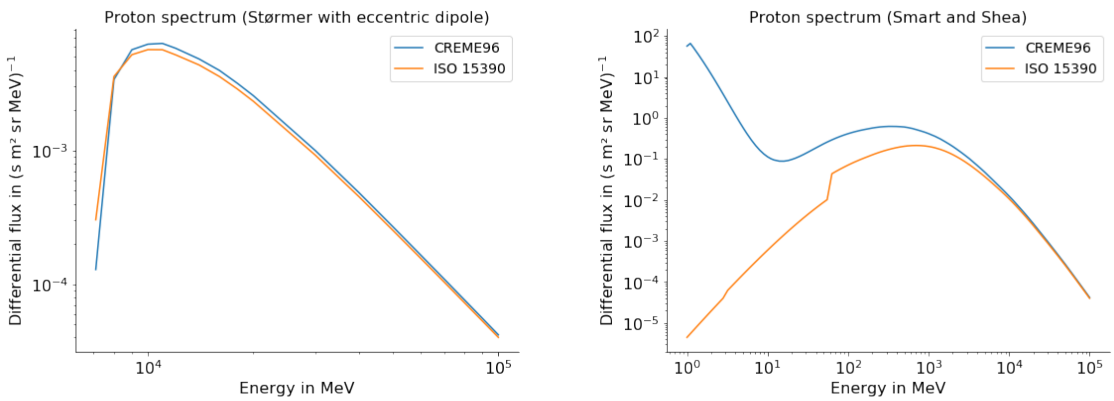

(a) Størmer magnetic shielding.

(b) Smart and Shea magnetic shielding.

Figure 3.14: Possible input proton spectra for the simulations. (a)Proton spectra of CREME96 (1) and ISO 15390 (2) models using the Størmer magnetic shielding method. The maximal flux is about $6 \times 10^{-3}\,(\mathrm{s\,m^2\,sr\,MeV})^{-1}$. (b) Proton spectra of CREME96 (3) and ISO 15390 (4) models using the Smart and Shea magnetic shielding method. The maximal flux is about $2.5 \times 10^{-1}\,(\mathrm{s\,m^2\,sr\,MeV})^{-1}$ for the ISO 15390 model. The local maximum of the flux for the CREME96 model is at about $8 \times 10^{-1}\,(\mathrm{s\,m^2\,sr\,MeV})^{-1}$ and the flux rises to low energies and reaches a value of about $7 \times 10^{1}\,(\mathrm{s\,m^2\,sr\,MeV})^{-1}$.

3.4 Background Spectra

3.4.1 Implementation of the Limited Energy Resolution

Several properties associated with the detector and the readout cause a limited energy resolution of the recorded spectra. Since this is not considered by the simulation, the limited energy resolution of the detector must be implemented afterwards.

The output of the simulation is implemented as a CSV file, which contains the deposited energies in the detector for each event. With this data a spectrum can be created in form of a histogram of the deposited energies. For this, a bin size in form of an energy range must be chosen. This bin size limits the energy resolution of the spectra resulting directly from the simulations. A fine binning can be useful to identify fluorescence lines because a small bin size gives very sharp lines. But in reality, these lines are broadened by the energy resolution of the detector, which depends on the measured photon energy.

The mean values of the energy resolution measurements of the SDDs used for the WFM, which are shown in Figure 3.16a, can be used as reference values for the LAD since it also consists of SDDs. To get the energy resolution for each detected energy value, a function was determined by fitting a root function to selected points of Figure 3.16a. To estimate the energy resolution for higher energies, this fitted function was extrapolated up to 80 keV. The selected points and the fitted curve including the extrapolation can be seen in Figure 3.16b.

The method of considering the detector's energy resolution chosen for this work is to create a Gaussian distribution based on the detector's measured energy resolu-

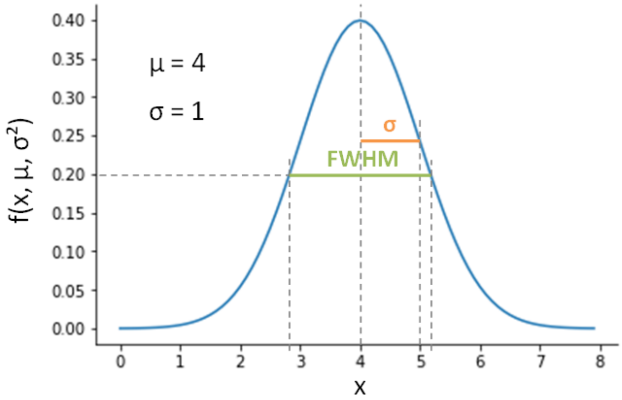

Figure 3.15: Gaussian distribution for a mean value $\mu = 4$ and a standard deviation $\sigma = 1$. There is a relation between the full width at half maximum (FWHM) and the standard deviation: FWHM $\approx 2.3548 \cdot \sigma$.

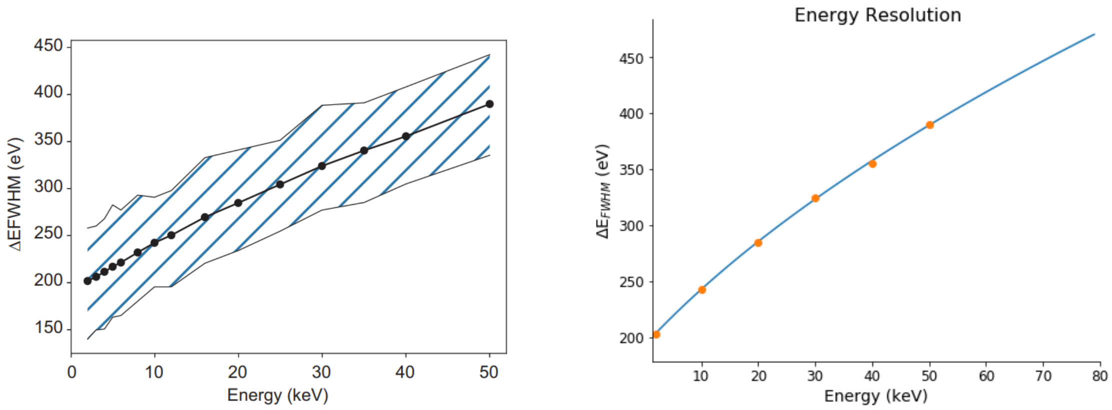

(a) Energy resolution of the WFM SDDs.

(b) Extrapolation of WFM energy resolution.

Figure 3.16: Determining a function of the energy resolution $\Delta E_{FWHM}(E)$ for SDDs where E is the photon energy. (a) The black dots represent the resolution values averaged on the whole SDD channel while the shaded area shows the range of energy resolution for each photon energy (Zhang et al. 2019). (b) Data points (orange) extracted from (a) that were fitted and extrapolated up to 80 keV (blue).

tion for every single energy value and draw a random number from this distribution to replace the original energy value. This leads to a Gaussian broadening of the spectral lines. In Python this can be done with the *numpy.random.normal*(E, σ) function where E is the energy value and, since the energy resolution is given by the FWHM (full width at half maximum), σ is calculated by the corresponding energy resolution divided by 2.3548, an approximation of the factor that relates the two variables (see Figure 3.15). Thus the Gaussian distribution is linked with the energy resolution and thus with the measured energy and the spectra can be provided with the energy resolution of the detector.

3.4.2 CXB Induced Background Spectrum

After creating the histograms from the CSV files of the simulations, the spectra have to be normalized as explained in Section 2.3.2 since the histograms only show

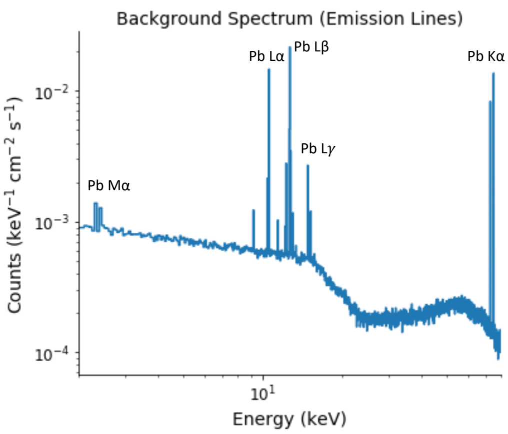

(a) Emission lines at ideal resolutuion.

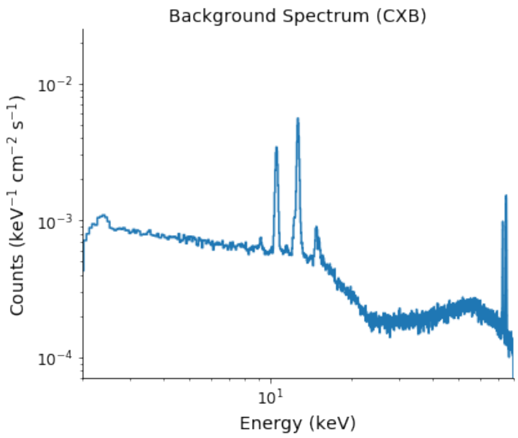

(b) Spectrum at realistic energy resolution.

Figure 3.17: The CXB induced LAD background spectrum simulated with 8 billion photons (a) The spectrum with an energy resolution only limited by the chosen bin size of 50 eV. Due to the high resolution, the fluorescence emission lines from materials used in the LAD module itself are sharp and clearly visible. (b) The CXB background spectrum at limited energy resolution of the LAD (see Section 3.4.1). The emission lines are broadened but still visible.

how many photons were detected at certain energies. Therefore, to get comparable spectra, the fluxes must be normalized to observation time and sensitive detector area. As also described in Section 2.3.2 (Equation 2.3) the simulated observation time relates to the number of simulated particles and the input spectrum. The simulation with 8 billion photons of the cosmic X-ray background, which is equivalent to a time of 12891 s in orbit, was performed with the LAD geometry using the lead glass bulk of reduced density instead of the capillary plate. The sensitive detector area of one LAD module of 1382.4 cm^2 is given by the sum of the areas of the SDDs.

Figure 3.17 shows the normalized spectra which only differ in the energy resolution. The energy resolution of the spectrum in Figure 3.17a is only limited by the bin size of 50 eV and therefore many emission lines can be resolved. These lines are fluorescence emission lines coming from the lead that is contained in the collimators and the lead shield. The emitted energy amount depends on the atomic electron transitions where an electron relaxes to its ground state on a lower shell. The first but rather weak emission lines at round 2.3 keV and 2.4 keV are caused by the $M\alpha_1$ and $M\alpha_2$ transitions of lead. The L-shell lines of lead from 9.2 - 14.8 keV and especially the $L\alpha$ and $L\beta$ lines around 10.5 keV and 12.5 keV are very prominent in the spectrum. At the high energy edge of the spectrum the $K\alpha$ lines can be clearly seen at 73 keV and 75 keV. With the limited energy resolution of the SDDs (see Figure 3.17b) these emission lines become blurred but they are still observable and increase the background flux at the corresponding energies.

Considering the whole spectrum, the average differential background flux level generated by the CXB is about $3.3 \times 10^{-4} \frac{counts}{\mathrm{s\,cm^2\,keV}}$. It can be seen that the spectrum is divided into two parts, the one at lower energies is above and the other is below this average level, as Figure 3.17 shows. The drop is after the L-shell emission lines

Table 3.5: Parameters used to normalize the resulting spectra of three different models: (1) CREME96 model with Størmer shielding, (3) CREME96 model with Smart & Shea shielding and (4) ISO 15390 model with Smart & Shea shielding.

Parameter	Value
Sensitive Detector Area	1,382.4 cm^2
Simulated Time:	
(1)	193,751 s
(3)	13,002 s
(4)	24,292 s

at around 15 - 20 keV. Especially these L-shell emission lines generate high fluxes at the energies around 10.5 keV and 12.5 keV. To consider each detected event, the total flux, which is the sum of all counts per second and square-centimeter, can be taken as a reference value. The flux can be calculated by integrating the differential flux over the energy range of the spectrum. This gives a value of $2.55 \times 10^{-2} \frac{counts}{\mathrm{s\,cm^2}}$ for the spectrum shown in Figure 3.17b.

3.4.3 GCR Induced Background Spectrum

The simulations of the detector background induced by the protons of the cosmic galactic rays were performed for three different models as described in Section 3.3.3. Since the LAD geometry is the same as the one for the previous CXB simulations, the normalization was implemented using the same sensitive detector area but a different observation time that has to be calculated for each input spectrum separately. These normalization parameters for simulations of 70 million protons are summarized in Table 3.5.

Figure 3.18 shows the normalized spectrum where Figure 3.18a shows one high resolution spectrum with four emission lines and the spectra in Figure 3.18b are the results of the different models with implemented energy resolution of the LAD. There is a significant difference between the intensity of the background fluxes obtained by the different models. The highest detector background flux is reached with the CREME96 model and the Smart & Shea magnetic shielding (3) whereas the same model but with the stronger Størmer shielding (1) leads to the lowest detector background flux.

The high resolution background spectrum, where the energy resolution is only limited by the bin size of 50 eV, shows four fluorescence emission lines also coming from lead, which is contained in the collimators and the lead shield (Figure 3.18a). Two lines at 10.55 keV and 12.65 keV are caused by the $L\alpha$ - and $L\beta$ - shell transitions. The other two lines at higher energies of about 73 keV and 75 keV are due to the $K\alpha$ transitions. These lines vanish by implementing the realistic energy resolution of the SDDs as it can be seen in Figure 3.18b.

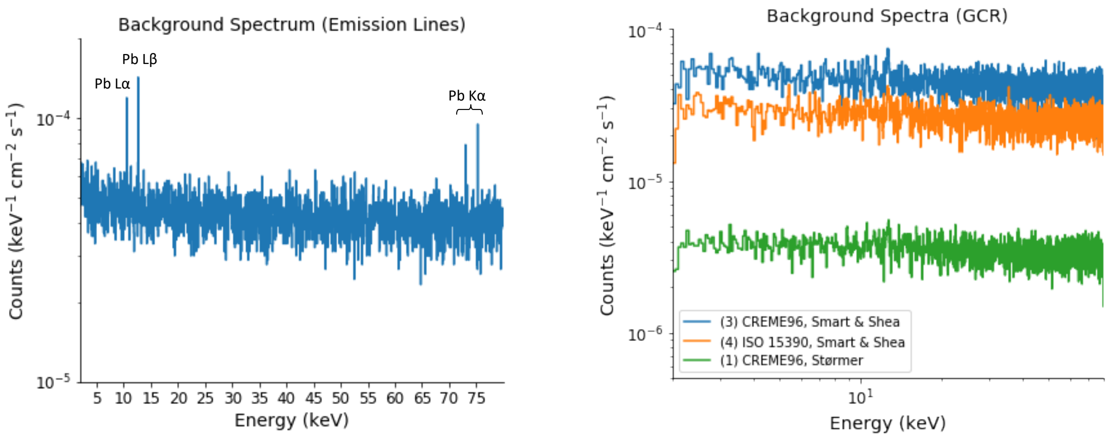

(a) Emission lines at ideal resolutuion.

(b) GCR background spectra.

Figure 3.18: The GCR induced LAD background spectrum simulated with 70 million protons (a) The spectrum, which was simulated with the CREME96 model and Smart & Shea shielding (3), with an energy resolution only limited by the chosen bin size of 50 eV. Four emission lines stand out from the rest of the spectrum. (b) The emission lines vanish when the limited energy resolution of the LAD is considered. The figure shows the background spectra for the three different GCR models used for the simulations.

Table 3.6: The average differential flux and the total flux of the spectra resulting from the simulations of three different models: (1) CREME96 model with Størmer shielding, (3) CREME96 model with Smart & Shea shielding and (4) ISO 15390 model with Smart & Shea shielding.

Model	Average Differential Flux in counts/(s cm^2 keV)	Total Flux in counts/(s cm^2)
(1)	3.43×10^{-6}	2.67×10^{-4}
(3)	4.32×10^{-5}	3.37×10^{-3}
(4)	2.58×10^{-5}	2.01×10^{-3}

Although the spectra resulting from the different models differ in the strength of the flux due to different amount of magnetic shielding they represent, the flat shape of the spectra is similar. The average differential fluxes and the total fluxes of the three different resulting spectra are summarized in Table 3.6.

3.4.4 Total Background Spectrum

The previously presented spectra are only constituents of the total detector background. To get an idea of the total background spectrum, which contains further minor contributions that are not considered in this work, the sum of the CXB and the GCR induced background spectra is determined, which makes up most of the detector background induced by radiation in orbit. When talking about the total background spectrum in this work, it is referred to the sum of the background flux caused by the photons (CXB) and the one caused by the protons (GCR). Since there

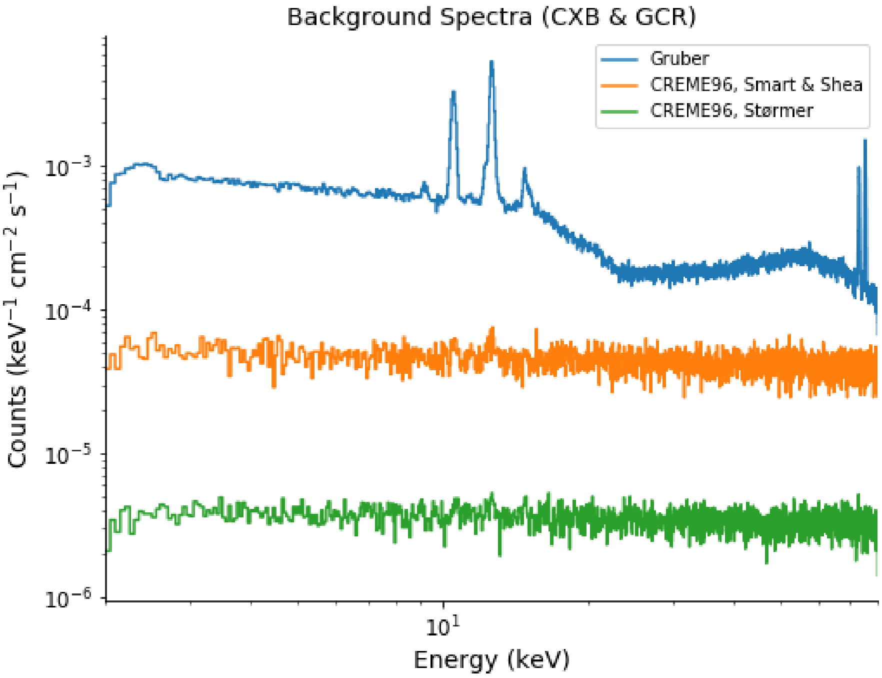

Figure 3.19: The single components of the total background spectrum. In blue is the spectrum induced by the CXB spectrum introduced by Gruber et al. (1999). Two of the GCR spectra are shown. To consider the diversity of the GCR spectra, the case of the highest and of the lowest proton induced background will be considered.

are several possible proton background spectra due to the different models, first the spectrum with the highest flux and then the spectrum with the lowest flux are added to the CXB generated spectrum. Therefore, the minimum and the maximum case can be considered. The components used to create the total background spectra are presented in Figure 3.19, which gives an idea how strong the individual background fluxes are in comparison to each other. The calculated background fluxes and average differential flux levels of these three spectra are summarized in Table 3.7.

The total background spectrum is presented in Figure 3.20. It shows that the different proton models do not cause significant changes in the detector background spectrum. Only a small increase can be observed as it is dominated by the CXB photons. The values of the average differential flux and the total flux of both background spectra are presented in Table 3.8 and show the small variations more precisely.

In order to be able to evaluate the results, they are compared with the requirement of a LAD background to be smaller than 10 mCrab (Zhang et al. 2019) in the main mode which is for the energy range of 2 - 30 keV (the extended mode is from 30 - 80 keV). One Crab is defined by the flux of the Crab Nebula in a certain energy range. The Crab Nebula is used as a standard candle to perform the calibration of various X-ray satellites (Kirsch et al. 2005).

In order to compare the detector background spectra resulting from the simulation studies, a value in units of counts/(s cm^2 keV) instead of mCrab is needed. For this purpose, the crab spectrum is simulated as a source and its spectrum measured

Table 3.7: The average differential flux and the total flux of the three different components which are later combined to the total detector background. The components are the CXB and the GCR induced background with two different models: (1) CREME96 model with Størmer shielding and (3) CREME96 model with Smart & Shea shielding.

Model	Average Differential Flux in counts/(s cm^2 keV)	Total Flux in counts/(s cm^2)
CXB	3.30×10^{-4}	2.55×10^{-2}
GCR(1)	3.43×10^{-6}	2.67×10^{-4}
GCR(3)	4.32×10^{-5}	3.37×10^{-3}

by the LAD can then be compared with the detector background spectrum. Since the rays from observed sources only arrive from one direction, a photon beam is taken as the primary particle source. In this case, the LAD geometry with the lead-glass bulk of a reduced density used instead of a capillary plate is not the optimal choice. The collimator properties of the lead-glass bulk change when particles are coming only from the direction the detector is pointing at and not from a spherical particle source surrounding the detector. For this purpose, it is better to use a capillary plate with the correct pore size of the LAD collimator pores for the simulations. Therefore, the small (around $2 \times 2\,\mathrm{cm}^2$) detector geometry with micro pores of 83.06 µm is used for the simulations. The photon beam is generated to hit a $1 \times 1\,\mathrm{cm}^2$ area on the detector perpendicularly.
The flux of the Crab spectrum can be approximated by a power law

$$F = N \cdot E^{-\Gamma} \tag{3.3}$$

with the normalization N in $\mathrm{s}^{-1}\,\mathrm{cm}^{-2}\,\mathrm{keV}^{-1}$ and the parameter Γ that are determined by various observations (Kirsch et al. 2005). Mean values of those parameters were chosen ($N = 9$, $\Gamma = 2.1$) to generate the Crab spectrum for the simulation.
The Crab observation was simulated with 1 million photons of the Crab spectrum. Only the photon flux Φ calculated from the Crab spectrum and the number of simulated photons N_s are needed to normalize the resulting spectrum because this time a beam was simulated and not an isotropic flux. The beam itself is already normalized and the spectrum resulting from the simulation can be normalized by dividing the counts by $\frac{N_s}{\Phi}$. Since the requirement of the LAD background is 10 mCrab the flux is also divided by a factor of 100.

Figure 3.20 includes the normalized spectrum resulting from the observation of the Crab spectrum (gray) together with the total detector background spectra (blue & orange). It shows that the detector background is lower in an energy range of 2 - 10 keV and is higher than the measured flux of the Crab spectrum at higher energies. To compare the total fluxes, they were calculated for an energy range of 2 - 30 keV since the Crab spectrum was limited to this energy range. These count rates are listed in 3.9. It shows that both detector background count rates fulfill the 10 mCrab requirement.

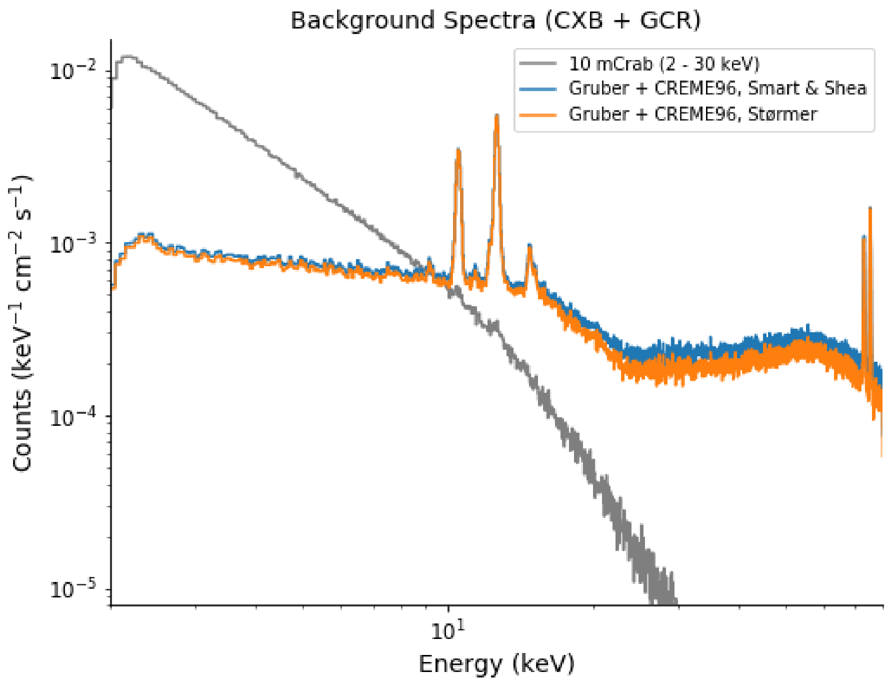

Figure 3.20: The total LAD background spectra that represent the sum of the CXB and GCR background. The blue spectrum represents the worst case detector background of the simulation results while the orange spectrum represents the best case. To compare the detector background spectra with the LAD background requirements of $< 10\,\text{mCrab}$, a 10 mCrab source was simulated and the resulting spectrum is shown in gray.

Table 3.8: The average differential flux and the total flux of the total background spectrum, which was created by adding the CXB induced background and the GCR generated background for two models for comparison: (1) CREME96 model with Størmer shielding and (3) CREME96 model with Smart & Shea shielding.

Model	Average Differential Flux in counts/(s cm^2 keV)	Total Flux in counts/(s cm^2)
CXB + GCR(1)	3.31×10^{-4}	2.58×10^{-2}
CXB + GCR(3)	3.71×10^{-4}	2.89×10^{-2}

Table 3.9: Total flux in the energy range of 2-30 keV of the total background spectra, which was created by adding the CXB induced background and the GCR generated background for two models: (1) CREME96 model with Størmer shielding and (3) CREME96 model with Smart & Shea shielding, and a 10 mCrab spectrum measured by the LAD.

Model	Total Flux (2-30 keV) in counts/(s cm^2)
CXB + GCR(1)	1.61×10^{-2}
CXB + GCR(3)	1.49×10^{-2}
10 mCrab	2.59×10^{-2}

3.4.5 Background Spectrum and Detector Thickness

In a further study the influence of the detector thickness on the detector background spectrum was investigated. Therefore, the same LAD geometry was used but the thickness of the silicon bulks, which are used as the detectors, were changed. Since the thickness used for the SDDs of the LAD is 450 µm, two additional simulations were done with thicknesses of 300 µm and 600 µm to study the influence of a thinner and a thicker detector.

First, the simulation of the different detector geometries exposed to the CXB was done with 1 billion photons. The resulting detector background spectra were normalized and are presented in Figure 3.21a. It shows that the CXB induced background level increases with the detector thickness. More precisely, related to the background of the 450 µm detector the flux is reduced to 76% for the 300 µm detector and with the 600 µm thick detector it is increased to 124%. The reason for this behavior is that a larger sensitive volume, which comes with an increasing detector thickness, offers more possibilities for interactions of particles with the detector. Therefore, more particles are detected and contribute to the detector background.

The simulation with 70 million protons of the GCR results in a different correlation (Figure 3.21b). In an energy range of about 2 - 60 keV the detector background flux seems to be independent of the detector thickness. However, the background flux in the 300 µm thick detector increases rapidly for energies above 60 keV. To explain this behavior the spectra were plotted up to 200 keV where the other detector geometries show a similar increase. The 450 µm thick detector observes an increase at about 100 keV and the 600 µm thick detector shows this behavior at about 140 keV. A possible explanation is a larger number of possible interactions of the high energetic protons in the detector when they are crossing more volume, which is the case for a thicker detector. As dE/dx is a constant for high energetic particles, the deposited particle energy is a function of the detector thickness. This leads to a total amount of deposited energy per event that is higher for a thick detector than for a thin detector. This means that the high background flux for the 300 µm detector starts at lower energies (because less energy is deposited) than for the 450 µm and 600 µm detectors (where a higher amount of energy is deposited).

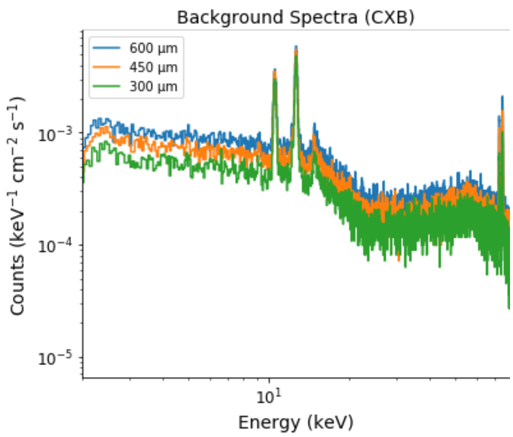

(a) CXB background spectra.

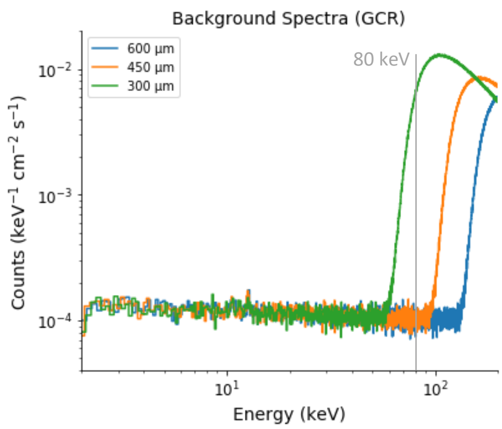

(b) GCR background spectra.

Figure 3.21: The figures show the simulation studies of the dependence of the detector background on the detector thickness. The actual thickness of the LAD SDD silicon layer is 450 µm. Therefore, a thicker (600 µm) and a thinner (300 µm) layer were simulated additionally. (a) The CXB background, simulated with 1 billion photons, becomes lower with a thinner detector. (b) A thinner detector leads to a high GCR background, which was simulated with 70 million protons of the CREME96 model with Smart & Shea shielding, at high energies of the detectable energy range of the LAD (2-80 keV).

In summary, the detector background flux caused by the CXB photons would decrease with a thinner detector, but then the background flux induced by the GCR protons would increase at the high energy end of the spectrum. In turn, a thicker detector leads to a higher detector background induced by photons but shifts the increase of the detector background caused by protons to higher energies. Since this increase is at about 100 keV for the detector with the medium thickness and the LAD only observes up to 80 keV, the chosen size of 450 µm provides a suitable solution to keep the total detector background as small as possible.

3.5 Conclusion

The simulation studies of one LAD module exposed to background radiation including photons of the cosmic X-ray background and high energy protons of the galactic cosmic rays were made to estimate the detector background that limits the sensitivity of the LAD observations.

The simulation results show that the main component contributing to the detector background is the one caused by the CXB. Protons of the GCR have less impact on the detector background, but they also contribute. Since there are several models of the GCR proton radiation, three of them where used for the simulations and the minimal and the maximal case were considered to calculate the total detector background caused by the CXB and the GCR. The difference of the total fluxes of the total detector background in an energy range of 2 - 80 keV was a change from 2.58×10^{-2} to 2.89×10^{-2} counts/(s cm^2). The specification for the detector background of the LAD is that it should remain below 10 mCrab for an energy range of 2 - 30 keV which is fulfilled according to the simulation results of this work.

Previous Monte Carlo simulations of the detector background for the LAD on board LOFT were made by Campana et al. (2013). Here, further components contributing to the detector background, such as the albedo γ-ray background or radiation caused by natural radioactivity of the isotope ^{40}K, which is contained in the lead-glass collimators in small fraction, were considered in the simulations. But the results show that the main component is also due to the photons of the CXB. Comparing the total fluxes of this work and the work of Campana et al. (2013) shows that the determined detector background is about 2×10^{-3} counts/(s cm^2) higher than the one simulated for the LAD of LOFT. Likewise, the 10 mCrab flux presented by Campana et al. (2013) is also higher, which could be an indication that this difference in detector background is due to different geometries used for the simulations.

The simulation environment is ready for further simulation studies such as the effects of geometry changes on the detector background. First studies of this kind were made to check the relation between the detector thickness and the detector background. This has led to the conclusion that the selected detector thickness is the right choice and a thicker or thinner detector would increase the detector background.

Chapter 4

HERMES Simulation Studies

The second key element of the simulation studies in this work is HERMES, which is a nano-satellite constellation hosting X- and gamma-ray transient monitors. More information about the HERMES mission is given in the following section, followed by an introduction to the science that will be at the core of the program with a particular focus on gamma-ray bursts (GRBs), which are the main sources observed by HERMES. In order to estimate the detector background, similar simulation studies as for the LAD were performed. The details, such as the implemented geometry of the HERMES satellite for the simulation and the input spectra of the particles inducing the detector background, are explained in more detail in this chapter. Furthermore, a GRB observation was simulated to obtain the measured flux and to compare it with the detector background.

4.1 The HERMES Mission

The High Energy Rapid Modular Ensemble of Satellites (HERMES) mission is a European project consisting of a swarm of nano-satellites, which are based on CubeSat[1] units. The satellites will permit the localization of transient high-energy events by triangulation and to study the temporal variations and spectral properties of these events, such as GRBs and the electromagnetic counterparts of Gravitational Wave Events (GWEs). First, a pathfinder mission of only six nano-satellites will be launched in mid-2020 to verify the functionality of the technology. The information presented here about the HERMES mission is based on Fuschino et al. (2018).

4.1.1 Mission Concept

HERMES differs from many other observatories in the required costs and development time. Since the nano-satellites are constructed from simple, but also innovative, $10\times10\times10\,\mathrm{cm}^3$ units, their development is more time-efficient and cost-effective. Tens to hundreds of these satellites will be distributed over the sky on low Earth orbits (LEOs) with different inclinations (Figure 4.1). The impact of the South

[1]The CubeSat project started in 1999 as a collaboration between the California Polytechnic State University and Stanford University's Space Systems Development Laboratory to create a standard for small satellite design that reduces cost and development time, improves accessibility to space, and supports frequent launches. A CubeSat is a 10 cm cube with a weight of up to 1.33 kg. (http://www.cubesat.org/)

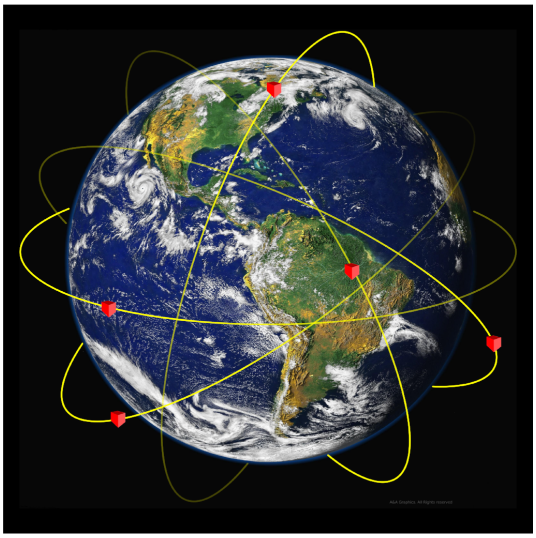

(a) Constellation of nano-satellites.

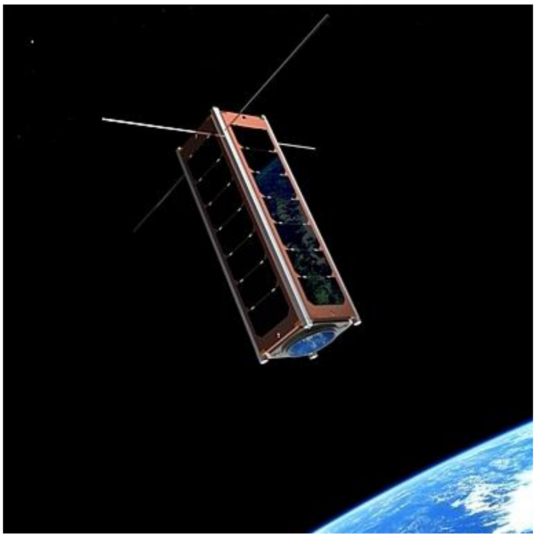

(b) 3 units Cubesat satellite.

Figure 4.1: Impressions of the HERMES mission. (a) Illustration of the HERMES nano-satellites in low Earth orbits with different inclinations (http://hermes.dsf.unica.it/). (b) A CubeSat satellite consisting of three units ($10 \times 10 \times 10\,\mathrm{cm}^3$ each unit) comparable with the design of the HERMES satellites (UKSA, ClydeSpace).

Atlantic Anomaly (see Section 3.1.1) on the satellite depends on the inclination of the satellite's orbit.

Since the HERMES detector has to fit into one CubeSat unit, its sensitive detector area is about $50\,\mathrm{cm}^2$, but with several tens/hundreds of such units a total sensitive area of the order of magnitude of about $1\,\mathrm{m}^2$ can be reached. The detector principle includes Silicon Drift Detectors (SDDs) combined with scintillator crystals to detect photons at higher energies where the SDDs are not sensitive anymore. This combination enables observations in a continuous energy range from keV to MeV. To localize transient high-energy events, the time delay of the event between detections by different nano-satellites is measured. The accuracy of the localization improves with the number of involved satellites.

4.1.2 Science with HERMES

With its capability of a wide sky coverage by several tens/hundreds of satellites and a sub-microsecond time resolution HERMES will permit:

- the accurate and prompt localization of bright hard X-ray/soft gamma-ray transients such as GRBs and to find the electromagnetic counterparts of GWEs by a prompt extensive sky search for transient high energy events with a negligible probability to find an uncorrelated event at the time of a GWE,
- investigation of the micro-second structure of GRBs,
- to test quantum space-time scenarios by measuring the delay time between GRB photons of different energies.

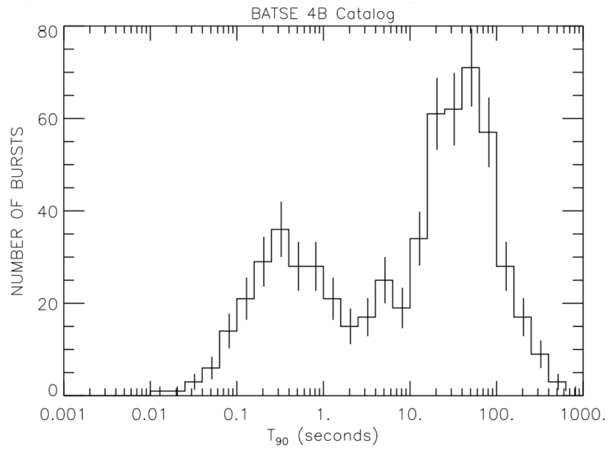

Figure 4.2: Duration distribution of GRBs detected with BATSE.
https://gammaray.msfc.nasa.gov/batse/grb/duration/

GRBs are the sources of interest because their observation combines studies of matter under extreme conditions, cosmology, fundamental physics and mechanisms of gravitational wave signal production. Therefore, an introduction of GRBs is given in the following paragraph with information based on Topinka (2009).

Gamma-Ray Bursts

GRBs are events of extragalactic origin that belong to the most luminous events known in the Universe. The short intense high-energy bursts can last from milliseconds to hundreds of seconds and are followed by afterglows at longer wavelengths.

The first GRBs were discovered by US satellites of the VELA program, which monitored the Earth's atmosphere for signs of nuclear weapon tests. But the event that was detected in 1967 did not come from the atmosphere. These gamma-rays came from outer space and belonged to the first observed GRB. In the 90s the Burst Alert and Transient Source Experiment (BATSE) on board the Compton Gamma Ray Observatory (CGRO) detected about 3000 GRBs, which led to major progress in understanding the GRB phenomenon. Further GRBs observatories followed.

The duration distribution of the observations shows that GRBs can be divided into two sub-groups: Short ($< 2\,\mathrm{s}$) and long ($\geq 2\,\mathrm{s}$) bursts. This separation becomes clearer with Figure 4.2, which shows the duration distribution where the GRBs accumulate in two distributions below and above 2 s, each with an average duration of about 0.3 s and 30 s, respectively. These two groups are thought to have different origins. Short bursts are probably produced by the fusion of two neutron stars to form a new black hole or a neutron star with a black hole that forms a larger black hole. The GRBs of long duration are likely to be caused by the formation of black holes in massive supernova explosions.

These very energetic events release a huge amount of energy in a very short time, which generates a very powerful jet. According to Courvoisier (2013) it is thought that powerful shocks are created by colliding elements in the jet as Figure 4.3 shows.

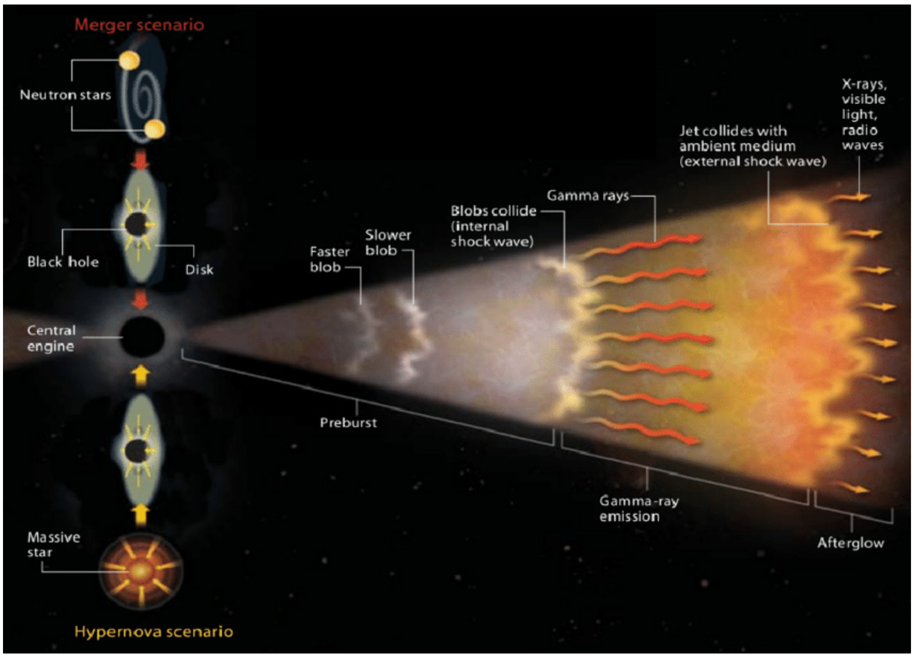

Figure 4.3: Illustration of the formation of a gamma-ray burst and the internal/external shock scenario. (Credit: NASA)

In these shocks electrons and positrons are strongly accelerated causing them to radiate through synchrotron and Compton processes. When the jet reaches the surrounding interstellar matter, new shocks are created that are thought to be the origin of the afterglow at longer wavelengths.

Although the light curves of the individual GRBs are quite different from each other, the spectra are similar in shape. Therefore, the GRBs spectra can be fitted by an empirical broken power-law function, which is called the Band-function (Band et al. 1993):

$$\begin{aligned} E \leq (\alpha-\beta)E_0 : \; & A\left(\frac{E}{100\,\mathrm{keV}}\right)^{\alpha} \exp\left(-\frac{E}{E_0}\right) \\ E > (\alpha-\beta)E_0 : \; & A\left(\frac{E}{100\,\mathrm{keV}}\right)^{\beta} \exp\left(\beta-\alpha\right)\left(\frac{(\alpha-\beta)E_0}{100\,\mathrm{keV}}\right)^{\alpha-\beta} \end{aligned} \tag{4.1}$$

where $E_P = (2+\alpha)E_0$ is the peak energy, A is the normalization factor at 100 keV in units of photons s^{-1} cm^{-2} keV^{-1}, α is the low-energy spectral power-law index, β is the high-energy spectral power-law index. An example spectrum can be found in Section 4.3.2.

4.1.3 HERMES Scientific Payload

One of the three CubeSat units of a HERMES nano-satellite is the payload unit shown in Figure 4.1a. It hosts the detectors in its center, the corresponding electronic boards on the bottom and a mechanical support, holding an optical filter, on the topside of the unit. A detailed view of the payload unit's components is shown in Figure 4.4b.

The detectors are a combination of SDDs and scintillator crystals. In total there are 120 SDD cells arranged in 12 tiles of 10 cells. Each SDD tile is located on top of 5 crystals, which means a total of 60 crystals. Soft X-rays are detected directly by being absorbed by the silicon. Hard X-rays and γ-rays induce optical scintillation light, which can be detected by the SDDs afterwards. Therefore, the detector unit is sensitive to photons of energies from 3-5 keV to 2 MeV with a sensitive area of $> 50\,\mathrm{cm}^2$ in this range. The scintillator crystals are made of a material with suitable characteristics: Cerium-doped Gadolinium-Aluminum-Gallium Garnet (Ce:GAGG), which combines characteristics as high light output ($\sim 50,000$ photons/MeV), no internal radioactive background, a fast radiation decay time of about 90 ns, and a peak light emission at 520 nm. Each GAGG crystal is coupled with two SDD channels, which leads to a uniform illumination of two SDD cells by the scintillator light. This allows to distinguish signals from the soft X-rays that are directly detected by the ten SDDs and are read out by only one channel. To study the temporal variability of GRBs and temporal coincidence between gravitational waves and their electromagnetic counterparts the electronics are designed to ensure a sub-microsecond timing resolution.
Further details and dimensions about the implemented HERMES geometry for the simulation studies are given in the next section.

4.2 Simulated HERMES Geometry

The HERMES geometry used for the simulations includes the satellite bus, the solar panel and the detector unit. The simulation geometry was created by Riccardo Campana at INAF/OAS in Bologna. Figure 4.5 gives an impression of the construction and its dimensions. Since the detector unit is the interesting part for the simulations, its individual components will be described in more detail. Figure 4.4b shows the components of the detector unit design. From this design the following components are implemented in the simulation geometry:

- 60 15 mm thick scintillator GAGG crystal bars.
- 120 SDDs realized by 450 µm thick silicon sheets.
- 6.5 mm thick collimator made of stainless steel.
- Two optical filters. The first filter layer is 1000 nm thick and consists of polyimide. The second filter is an 80 nm thick aluminum layer.
- 3 printed circuit boards (PCBs) made of a 1 mm thick composition of 60% silicon dioxide and 40% mixture of bisphenol A diglycidyl ether, 1,4-butanediol diglycidyl ether and 1,6-hexanediamine 2,2,4-trimethyl.
- An optical coupler of 1 mm thick silicone.

Furthermore, it includes tungsten layers for shielding and boxes in which the single components are hosted. The SDDs and the scintillators are arranged in 12 tiles as shown in Figure 4.6. The solar panel consists of a 2.1 mm thick aluminum layer and 0.4 mm thick silicon dioxide layer. A box with 5 mm thick aluminum walls was used for the satellite bus.

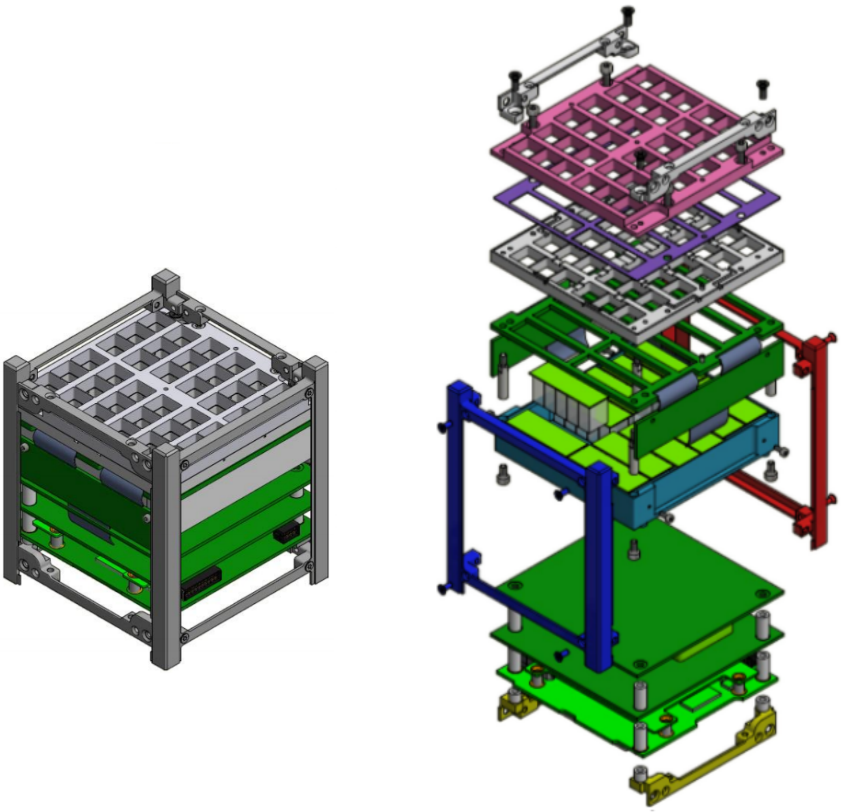

(a) Cubic detector unit. (b) Exploded view of the detector unit.

Figure 4.4: Detector unit on board the HERMES nano-satellite. (a) The compact $10 \times 10 \times 10\,\mathrm{cm}^3$ unit. (b) Detector components: From the top are shown the mechanical support composed by top (pink) and bottom (gray) parts, with optical filter (violet) in middle, the FEE board (dark green) allocating SDD matrices (light green), the GAGG crystal pixels (white transparent) and their housing (greenish blue). Mechanical ribs on top (gray) and on bottom (yellow) are also visible, necessary to fix the payload components to the satellite structure (blue and red). (Fuschino et al. 2018)

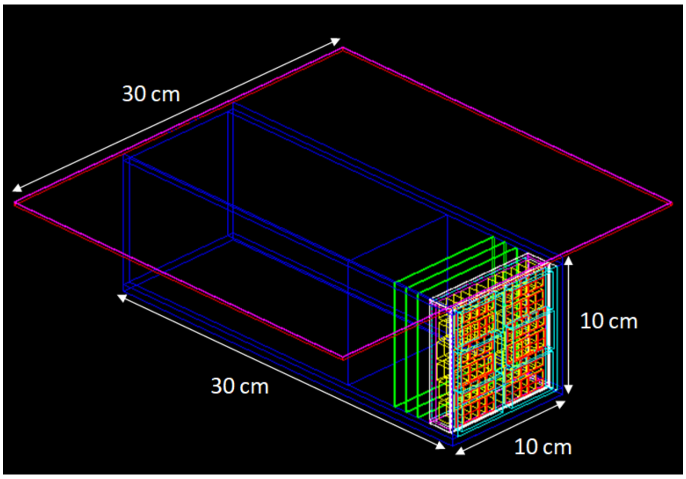

Figure 4.5: HERMES simulation geometry including the solar panel (pink), satellite bus (blue), PCBs (green), scintillator crystals (yellow) and SDDs (red).

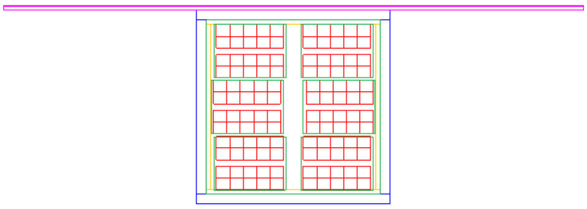

(a) Front view of the HERMES satellite geometry.

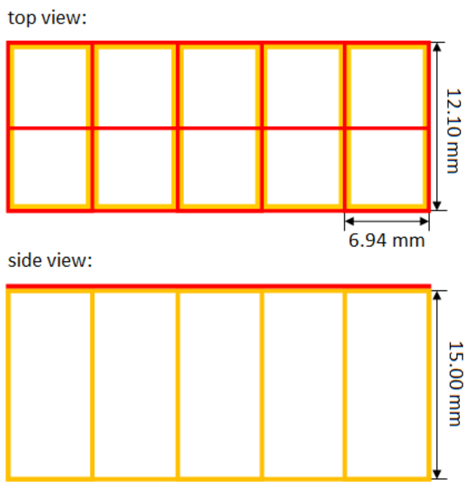

(b) One detector tile.

Figure 4.6: HERMES simulation geometry. (a) Satellite including components as the solar panel (pink), the satellite bus (blue) and the SDD cells (red). (b) A detector tile (red) includes ten SDD cells mounted on five scintillator crystals (yellow).

Table 4.1: Parameters used to create the low and high inclined spacecraft trajectories of HERMES in SPENVIS.

Parameter	Value
Altitude	600 km
Inclination	2.5° and 57°
Mission Duration	1 year
Orbit Start	01/01/2020

The SDDs and the scintillator crystals are defined as sensitive volumes to detect the photons, although in reality the SDDs are the only detector units and the scintillator crystals are for converting the high energy photons that cannot be absorbed by the SDD into optical photons. But as mentioned in Section 2.3.3 there is an energy threshold of 100 eV implemented in the physics list used for the simulations that limits the production of secondary particles and since the energy of the optical photons would be beneath this threshold they would not be created at all. Therefore, it is more efficient to define the scintillator crystals themselves as detectors.

4.3 Primary Particle Generation

The HERMES simulation studies performed for this work include studies of the detector background and of a simulated source observation. Therefore, the incoming particles that were considered in the HERMES simulations are:

- photons from the cosmic X-ray background (CXB),
- galactic cosmic ray (GCR) protons and
- photons coming from a gamma-ray burst (GRB).

4.3.1 Input Spectra for Background Simulation Studies

Since the CXB spectrum does not depend on the orbit of the satellite, the same spectrum can be used as for the eXTP LAD simulation, which was described in Section 2.3.1.

Due to the large number of planned satellites, which will be located on different LEOs, two possible orbits will be simulated to predict how this will affect the GCR induced background. One is a similar orbit to the LAD orbit with a low inclination and the second one has the same altitude as the first but a higher inclined orbit. The parameters used for HERMES to create both trajectories in SPENVIS are shown in Table 4.1.

The proton spectra created for the low inclination orbit are shown in Figure 4.7. It can be seen that three spectra resemble each other. These are the spectra created

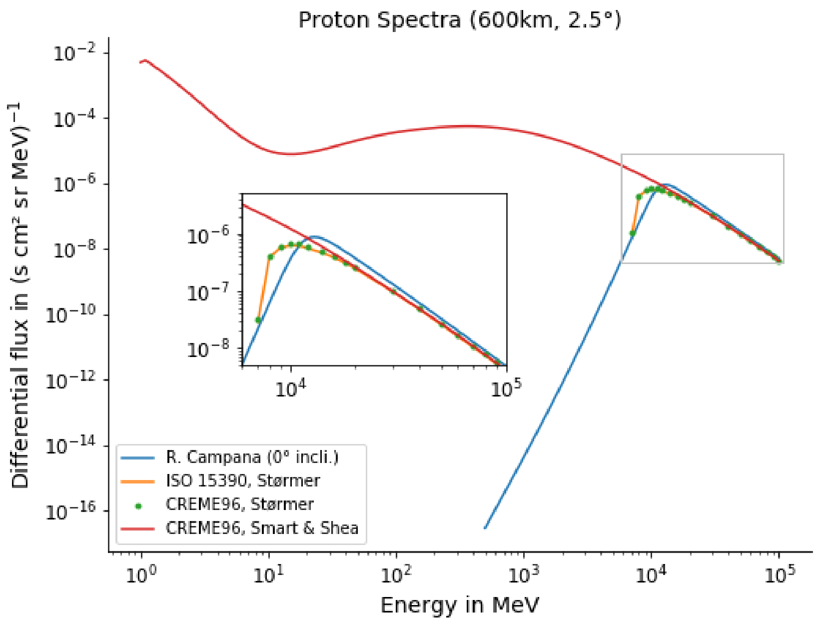

Figure 4.7: Spectra of different models that represent the GCR flux in an orbit of 600 km height and 2.5° inclination. The blue spectrum (1) was created by Riccardo Campana and is taken as a reference spectrum. The other three spectra were created using different models provided by SPENVIS. The CREME96 model with magnetic shielded defined by Smart & Shea (2) and by Størmer (3), and the ISO 15390 with the Størmer shielding (4) were used.

by Riccardo Campana with an inclination of 0°, the spectra created with the ISO 15390 and the CREME96 models with the Størmer magnetic shielding. Since the last two spectra are identical, only the CREME96 model with both cases of magnetic shielding and the spectrum by R. Campana were used for the simulations. Section 3.3 gives more information about the models and the magnetic shielding since they have already been used for the previous LAD simulations.

Figure 4.8 shows the spectra created for an orbit with an inclination of 57°. The simulations were done for the same models, which were used for the low inclination orbit. It can be seen that the magnetic shielding with the Størmer model has not the same effect on the more inclined orbit as on the low inclination orbit. More precisely, the shielding is weaker and therefore, the background is probably higher on this orbit.

4.3.2 GRB Input Spectrum for Source Simulation Studies

To simulate a GRB event observed by the HERMES detector in this work, a known GRB spectrum was fitted and implemented in the GPS macro file. The bright and well documented GRB 910503 was used to create this spectrum. It was observed on May 3rd, 1991 for about 10 s. A photon flux between 44 and 52 photons $s^{-1}\,cm^{-2}$ is

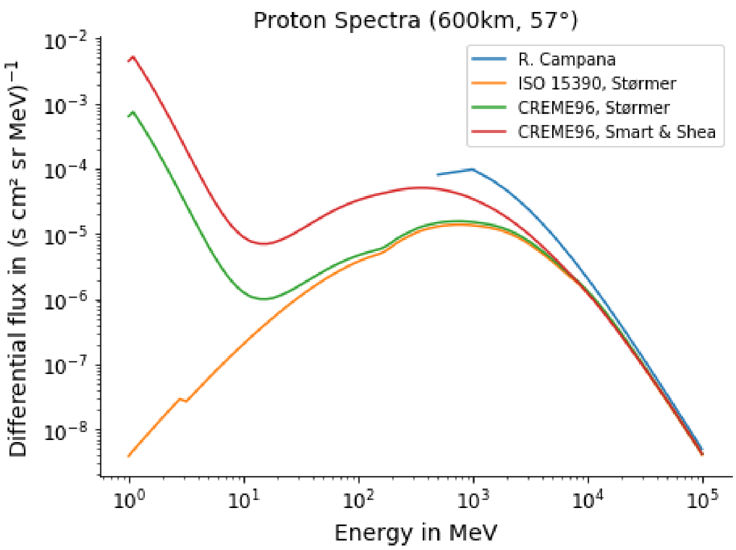

Figure 4.8: The GCR flux in an orbit of 600 km and 57° inclination created using different models. The blue spectrum (5) was created by Riccardo Campana and is taken as a reference spectrum. The other three spectra were created using different models provided by SPENVIS. The CREME96 model with magnetic shielded defined by Smart & Shea (6) and by Størmer (7), and the ISO 15390 with the Størmer shielding (8) were used.

listed in the Gamma Ray Burst Catalog[2]. For comparison, the brightest observed GRB photon fluxes can reach values above 100 photons s^{-1} cm^{-2} (Gruber et al. 2014). The spectrum of GRB 910503 is documented in Schaefer et al. (1998) where its data from the CGRO instruments, BATSE, Imaging Compton Telescope (COMPTEL) and Energetic Gamma Ray Experiment Telescope (EGRET), is combined. This data was fitted by the Band-function (Equation 4.1) multiplied by $\left(\frac{E}{100\mathrm{keV}}\right)^2$. Parameters of the Band-function were used from Kaneko et al. (2005) as a reference and adjusted further to find a suitable fit. The data points of the observed spectrum and the fitted function are shown in Figure 4.9a. Figure 4.9b shows the spectrum that was implemented in the GPS. It is the fitted function divided by $\left(\frac{E}{100\mathrm{keV}}\right)^2$ to get the spectrum in the required units of $(\mathrm{s\,cm\,keV})^{-1}$.

Since the source photons are coming from one direction, the spherical source, which was used to simulate the isotropic background, is replaced by a photon beam. This beam is chosen to be perpendicular to the detector's surface.

4.4 Results of the Simulation Studies

4.4.1 Implementation of the Energy Resolution

As described in Section 3.4.1 a real detector has a limited energy resolution. Since this property is not considered in the simulations, it must be implemented afterwards.

[2]https://heasarc.gsfc.nasa.gov/grbcat/

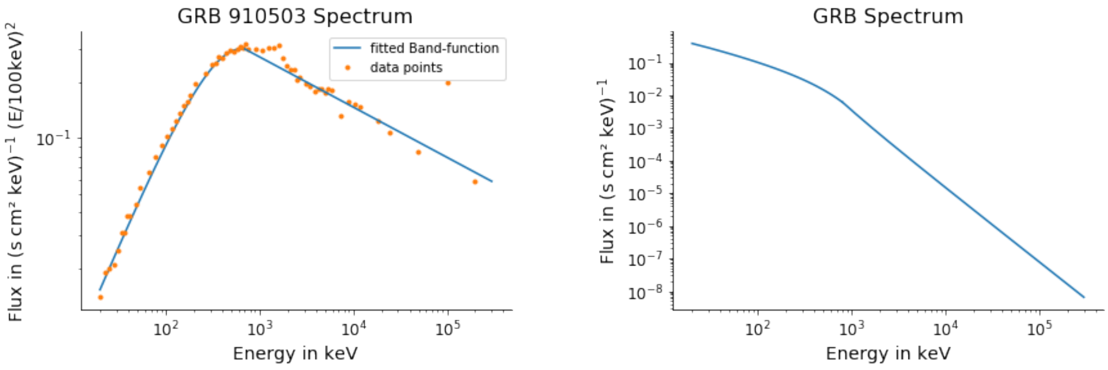

(a) Data points and fitted curve.

(b) Input spectrum for the simulations.

Figure 4.9: Spectra of GRB 910503. (a) The blue line represents the fitted Band-function multiplied by $\left(\frac{E}{100\text{keV}}\right)^2$, which is used to create the simulated input spectrum. The fitting parameters are $A = 0.11$ photons $\text{s}^{-1}\,\text{cm}^{-2}\,\text{keV}^{-1}$, $E_P = 630\,\text{keV}$, $\alpha = -0.8$ and $\beta = -2.27$. (b) The function used to create the GPS input spectrum. Both spectra only differ by a $\left(\frac{E}{100\text{keV}}\right)^2$.

The HERMES detectors consist of SDDs and scintillators that have different energy resolution properties. Therefore, different energy resolutions are defined for these two detector types. For the SDDs, the same energy resolution can be used as for the SDDs of the LAD (see Section 3.4.1 and Figure 3.16). For the events detected by the scintillator crystals, an energy resolution can be estimated by $\frac{\Delta E_{FWHM}}{E} = 12\%$ (Seitz et al. 2016), which means there is a linear relation between the detected energy E and the line width ΔE_{FWHM} in the energy range used in these simulations.

4.4.2 CXB Induced Detector Background

The histograms resulting from the output files of the simulations must first be normalized in order to obtain conclusive spectra. 8 billion photons of the cosmic X-ray background were simulated with the HERMES detector. This corresponds to an observation time of 28325.8 s in orbit. Dividing the absolute counts by this observation time and the sensitive detector area of $50.4\,\text{cm}^2$ gives the normalized detector background spectrum in Figure 4.10. Since the SDDs and the scintillators are sensitive at different energy ranges, the events of both detector types are first plotted separately to get more information. The SDDs are sensitive in the low energy range from 1 keV to about 60 keV. The sensitivity of the scintillator crystals starts at about 20 keV and reaches energies up to 2 MeV (Fuschino et al. 2018). Therefore, the sensitive energy ranges of both detectors overlap in the range of 20 - 60 keV and complement each other in the remaining range. These sensitive energy ranges will later be important in the calculation of the total background.

Figure 4.10a shows the CXB induced background spectra measured by the SDDs and the scintillators with an energy resolution only limited by the chosen bin size of 50 eV. Due to the high energy resolution the occurring fluorescence emission lines are sharp and can be identified.
The spectrum detected by the scintillator shows several emission lines, which are distributed over a wide energy range. All emission lines, including those below

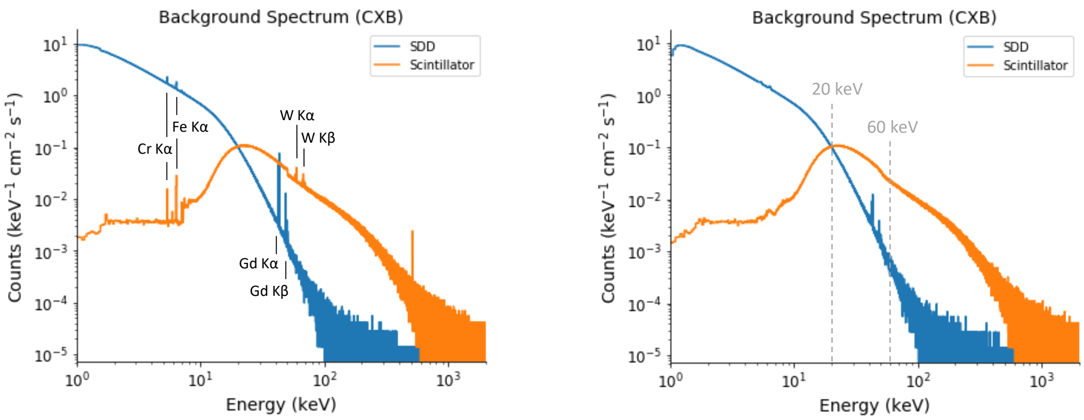

(a) Emission lines at ideal energy resolution. (b) Spectrum with realistic energy resolution.

Figure 4.10: The CXB induced HERMES detector background spectrum simulated with 8 billion photons. The background spectrum consists of two components: The photons detected by the SDDs (in blue) and the photons measured by the scintillator crystals (in orange) (a) The spectrum with an energy resolution only limited by the chosen bin size of 100 eV. Due to the high resolution, the fluorescence emission lines are sharp and clearly visible. (b) The CXB background spectrum at limited energy resolution of the SDDs and scintillator crystals (see Section 4.4.1). The emission lines of the SDD spectrum are weaker but still visible. The lower energy resolution of the scintillators flattens the emission lines.

20 keV, are considered and assigned to the materials to verify the accuracy of the simulation.
The first noticeable emission line is at about 5.4 keV where chromium has a fluorescence line coming from the $K\alpha$ transitions. Chromium is included in stainless steel, which is made of three components: 74% iron, 18% chromium and 8% nickel. Stainless steel is used for the collimators and the boxes that include the scintillator crystals of the HERMES detector. It is also the origin of the following emission lines in the range up to 7.5 keV, in this range each of the three material components has fluorescence emission lines. The prominent lines, which are detected by the scintillators and the SDDs, are the $K\alpha$ lines of chromium at around 5.4 keV and the $K\alpha$ lines of iron around 6.4 keV. The Cr $K\beta$ line is located between them at about 5.9 keV. These lines are followed by a collection of merging lines in the spectrum measured by the scintillators. This collection includes the iron $K\beta$ line at ~ 7 keV, nickel $K\alpha$ and $K\beta$ lines at ~ 7.5 keV and ~ 8.3 keV followed by lines of tungsten, which is used for the shielding, vanishing in the continuum.
At higher energies there are weaker emission lines produced by $K\alpha$ and $K\beta$ transitions of tungsten at around 58 keV, 59 keV, 67 keV and 69 keV.
At ~ 511 keV the scintillator detects an additional emission line that doesn't originate in shell transitions. γ-rays with energies > 1022 keV can produce electron-positron pairs by pair production. The annihilation of those positrons and electrons generates two photons of 511 keV that can be detected by the scintillator afterwards and lead to the emission line in the spectrum.
The SDDs detect high-energy fluorescence emission lines from the GAGG scintillator crystals, which are the lines caused by the $K\alpha$ and $K\beta$ transitions of gadolinium at around 42.3 keV, 43.0 keV, 48.7 keV and 50.0 keV. Since no distinction is made

between the different scintillator crystals in the detection of events, the spectrum measured by the scintillators does not contain the emission lines originating from the GAGG crystals themselves. Imagine a particle that triggers fluorescence in one scintillator crystal, i.e. it first deposits energy that is later released by a photon that leaves the crystal afterwards. It can then be detected by another scintillator crystal. In this case, the total energy deposition of this fluorescence process is zero for this event and no emission line occurs in the spectrum.

After identifying the emission lines, the realistic energy resolution of the detector is implemented, which makes most of the emission lines undetectable (Figure 4.10b). Only the $K\alpha$ and $K\beta$ shell transitions of gadolinium are still recognizable as emission lines.
Looking at the complete spectrum measured by the SDDs, it is noticeable that it is similar in shape to the CXB spectrum having a high flux at low energies that decreases towards low energies continually. At about 20 keV, when the flux measured by the scintillator reaches its maximum, both detector types measure the same amount of detector background counts. This is also the point where the flux measured by the scintillator exceeds the flux of the SDD and where the sensitive energy range of the scintillator begins.
Both spectra will later be combined (Section 4.4.4) when calculating the total detector background caused by the CXB and the protons of the GCR. Then, the first step is to combine the spectra measured by the SDDs and the scintillators considering their sensitive energy ranges of 1 - 60 keV and 20 - 2000 keV respectively.

4.4.3 GCR Induced Detector Background

The simulation of the GCR was performed with only 5 million protons due to the high computing time required to simulate high energy protons on the HERMES geometry. This also led to a smaller number of detected events that do not allow the same small bin size as for the CXB induced spectra. Figure 4.11 shows a spectrum, which results from one of the three GCR model simulations, that is only limited by the resolution of the bin size of 1 keV. Only the 511 keV emission line coming from electron-positron pair production and the annihilation afterwards (Section 4.4.2) is clearly identifiable. The fact that no further lines are visible doesn't imply the general absence of further emission lines, but the low statistics and the larger bin size could obscure them.

Since the GCR simulation studies for HERMES take two different orbits into account, the resulting spectra are also arranged in separate figures for each orbit. All normalization parameters needed to create the spectra resulting from the different models and orbits are listed in Table 4.2. Figure 4.12 shows the normalized spectra resulting from different GCR models at the low inclination orbit (2.5°). For a better visual overview, the spectra measured by the SDDs and scintillators are presented separately. Figure 4.13 shows the corresponding spectra for the high inclination orbit (57°). The detector energy resolution is already implemented for the presented spectra and it leads to an extinction of the 511 keV emission line. Looking at the flux measured by the SDDs it is important to consider the sensitive energy range of 1 - 60 keV where the spectra are rather flat. The increase of the flux starts out

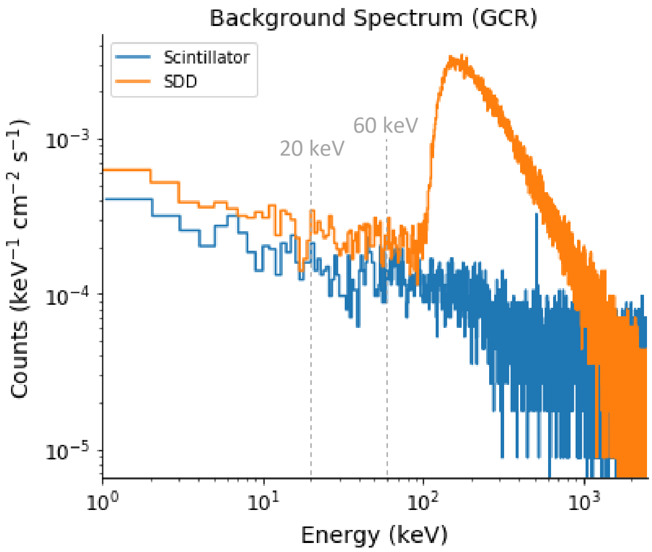

Figure 4.11: The GCR induced background at an energy resolution only limited by the bin size of 1 keV. One emission line can be seen at 511 keV. 5 million protons were simulated here with the CREME96 model with the Smart and Shea magnetic shielding. The big bump in the SDD spectrum corresponds to the typical energy that a proton deposits in the detector when crossing it completely.

Table 4.2: Parameters used to normalize the resulting spectra of three different models for the low inclination (2.5°) orbit: (1) spectrum by R. Campana at 0° inclination, (2) CREME96 model with Smart & Shea shielding and (3) CREME96 model with Størmer shielding, and three models for the high inclination (57°) orbit: (5) spectrum by R. Campana, (6) CREME96 model with Smart & Shea shielding and (7) CREME96 model with Størmer shielding

Parameter	Value
Sensitive Detector Area	50.4 cm^2
Simulated Time:	
(1)	25,062 s
(2)	2,249 s
(3)	29,349 s
(5)	1,289 s
(6)	2,344 s
(7)	4,012 s

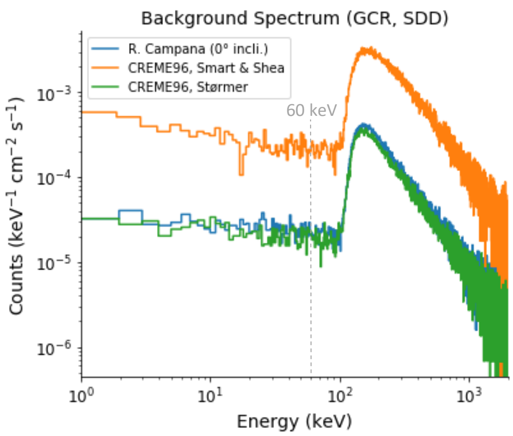

(a) SDD background.

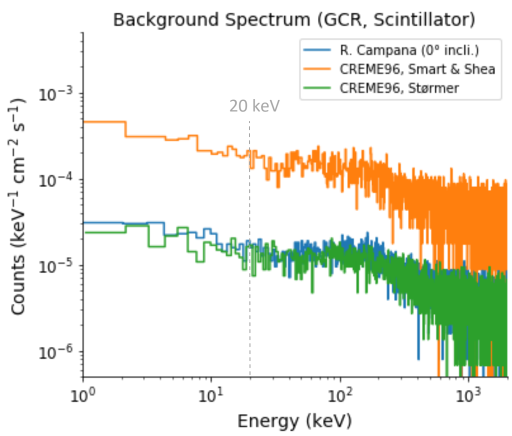

(b) Scintillator background.

Figure 4.12: The GCR induced HERMES detector background spectrum for an orbit of an altitude of 600 km and a low inclination of 2.5°. Three different models were simulated with 5 million protons. (a) The background spectra on the SDDs. (b) The corresponding background spectrum detected by the scintillator crystals.

of this sensitive energy range at around 100 keV. It is due to the typical energy loss of particles crossing the SDD completely. This increase can be compared to the behavior of the SDD of the LAD described in Section 3.4.5, where the GCR induced detector background of the SDD was shown up to 200 keV. The sensitive range of the scintillator starts at about 20 keV where the spectra are rather flat. Then, above 100 keV the scintillator background flux shows a slight decrease. This basic behavior of the flux is similar for both orbits. It is noticeable that the detector background of the orbit with low inclination is generally significantly lower than that of the orbit with high inclination except for the spectra created by the CREME96 model with the weaker magnetic shielding (Smart & Shea). These spectra show very small differences between the two orbits.
The values of the combined GCR induced spectra measured by the SDDs and scintillators are presented together with the CXB induced spectrum in the following section to compare the spectra directly and to create the total detector background.

4.4.4 Total Detector Background

In this section, the total detector background is determined for each of the two orbits. First, the SDD and the scintillator components are combined according to the respective sensitive energy ranges. Then, the total detector background induced by the CXB and the protons of the GCR can be determined.

Low Inclination Orbit

Figure 4.14 shows the CXB induced spectrum (in red) and the GCR induced spectra after the addition of the SDD and the scintillator components. It is clearly visible that the CXB induced spectrum dominates the detector background up to high energies where it converges to the GCR induced spectra. The spectra have edges where the sensitive energy range of the scintillators (20 keV) begins or that of the SDDs (60 keV) ends. Figure 4.15 shows the total background spectra that

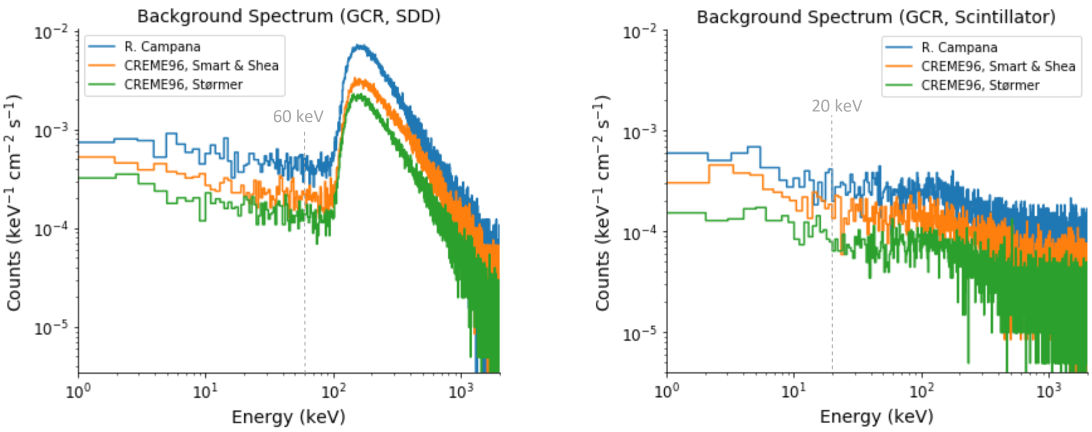

(a) SDD background.

(b) Scintillator background.

Figure 4.13: The GCR induced HERMES detector background spectrum for an orbit of an altitude of 600 km and a high inclination of 57°. Three different models were simulated with 5 million protons. (a) The background spectra on the SDDs. (b) The corresponding background spectrum detected by the scintillator crystals.

result from adding the CXB and the GCR components. Since three different models were used to obtain the GCR induced background flux, there are also three total background spectra. It can be seen that these spectra are similar since the CXB component dominates. The average differential flux and the total flux were calculated for each spectrum of both figures and are presented in Table 4.3, which also shows the domination of the CXB induced detector background.

High Inclination Orbit

The same procedure was followed for the results of the simulations of the high inclination orbit. Figure 4.16 shows the single components of the different background radiation origins. In Figure 4.17 these components are added together to get the total detector background. The values of the average differential fluxes and the total fluxes are summarized in Table 4.4 and show that the total detector background in the high inclination orbit is slightly higher than in the low inclination orbit.

4.4.5 Results of the Gamma-Ray Burst Observation

For the HERMES detector studies an additional simulation of a source observation in the form of a GRB was performed. Since GRBs are transient events, the number of photons to be simulated was adjusted to the duration of GRB 910503, which is 10 s. This leads to 17130 photons which are simulated by a beam that hits the detector perpendicularly. The normalization of the resulting spectrum can be done by dividing the counts by $\frac{N_s}{\Phi}$ with the number of simulated photons N_s and the photon flux Φ calculated from the GRB 910503 spectrum. Due to the low realistic number of simulated photons the resulting spectra have rather low statistics. Figure 4.18 includes the results detected by the SDDs and the scintillators and shows the total measured spectrum calculated by adding both components.

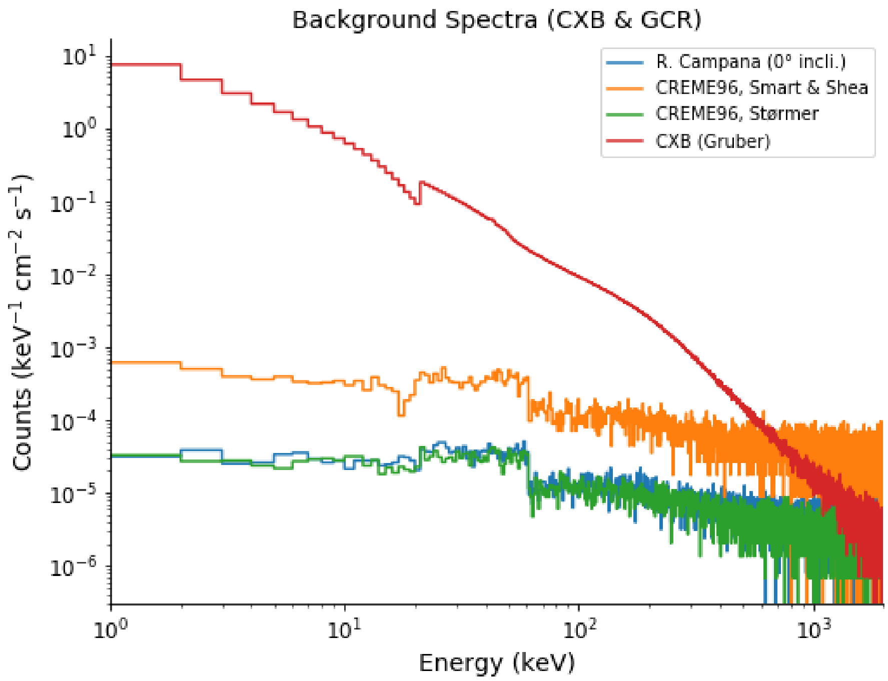

Figure 4.14: The single components of the total background spectrum on a low inclination orbit of 2.5°. The spectra resulting from the different GCR models are shown in blue (1), orange (2) and green (3). In red is the spectrum induced by the CXB spectrum introduced by Gruber et al. (1999).

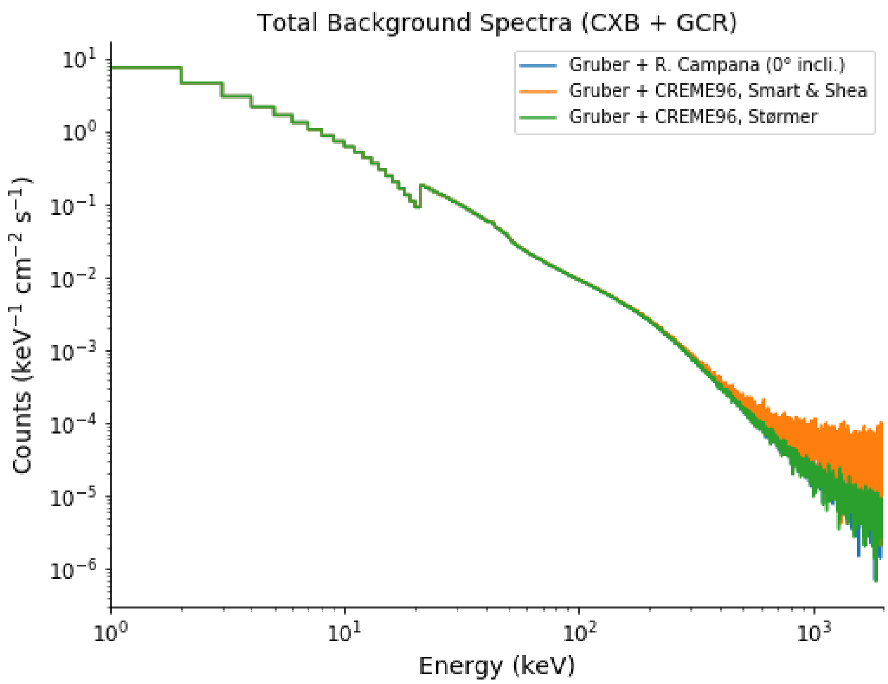

Figure 4.15: Total background spectra on a low inclination (2.5°) orbit. The spectra are determined by adding the spectra resulting from the CXB and the GCR simulations together. Due to the different possible GCR models there are three total background spectra which can be compared.

Table 4.3: The average differential flux and the total flux of the spectra resulting from the simulations of three different GCR models for the high inclination (2.5°) orbit: (1) spectrum by R. Campana at 0° inclination, (2) CREME96 model with Smart & Shea shielding and (3) CREME96 model with Størmer shielding. Also shown are the values of the total background spectra where the CXB and the GCR background are added together.

Model	Average Differential Flux in counts/(s cm^2 keV)	Total Flux in counts/(s cm^2)
CXB	1.52×10^{-2}	26.6
GCR(1)	5.99×10^{-6}	1.20×10^{-2}
GCR(2)	5.70×10^{-5}	1.14×10^{-1}
GCR(3)	5.11×10^{-6}	1.02×10^{-2}
CXB + GCR(1)	1.52×10^{-2}	26.7
CXB + GCR(2)	1.53×10^{-2}	26.8
CXB + GCR(3)	1.52×10^{-2}	26.7

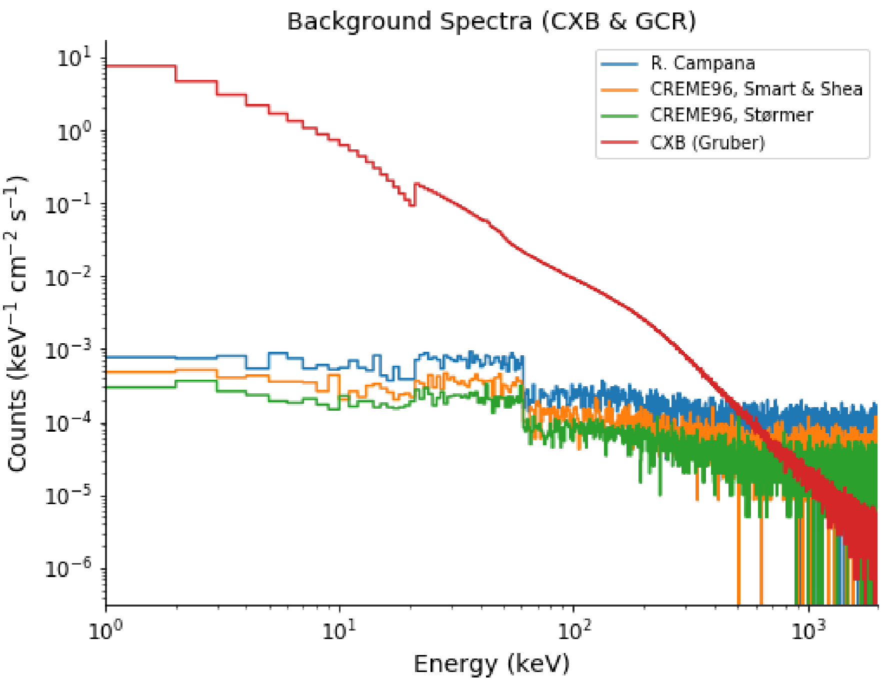

Figure 4.16: The single components of the total background spectrum on a high inclination orbit of 57°. The spectra resulting from the different GCR models are shown in blue (5), orange (6) and green (7). In red is the spectrum induced by the CXB spectrum introduced by Gruber et al. (1999).

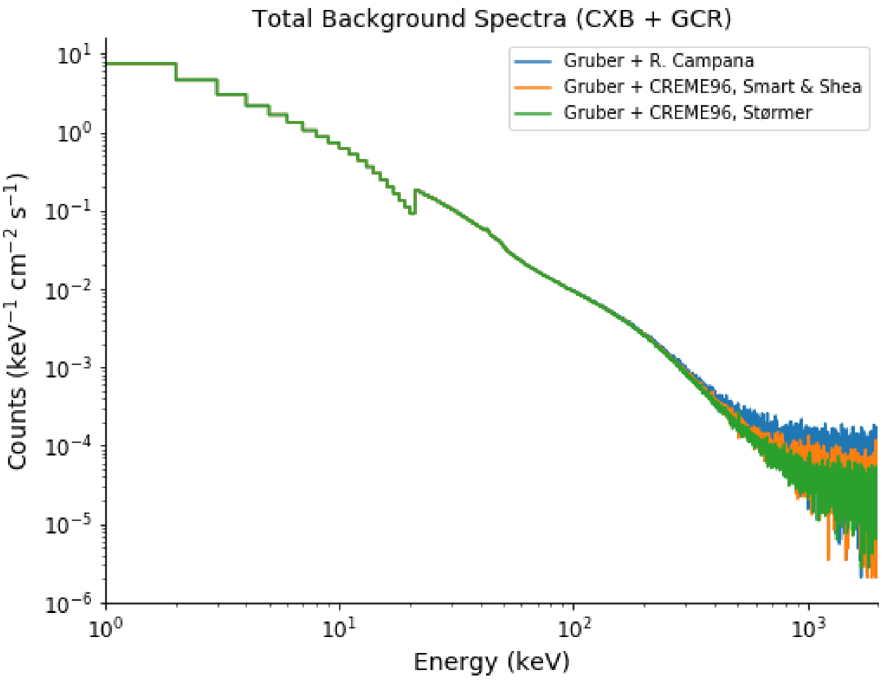

Figure 4.17: Total background spectra on a high inclination (57°) orbit. The spectra are determined by adding the spectra resulting from the CXB and the GCR simulations. Due to the different possible GCR models there are three total background spectra which can be compared.

Table 4.4: The average differential flux and the total fluxes of the spectra resulting from the simulations of three different GCR models for the high inclination (57°) orbit: (5) spectrum by R. Campana, (6) CREME96 model with Smart & Shea shielding and (7) CREME96 model with Størmer shielding Also shown are the values of the total background spectra where the CXB and the GCR background are added together.

Model	Average Differential Flux in counts/(s cm^2 keV)	Total Flux in counts/(s cm^2)
CXB	1.52×10^{-2}	26.6
GCR(5)	1.10×10^{-4}	2.20×10^{-1}
GCR(6)	5.64×10^{-5}	1.12×10^{-1}
GCR(7)	3.55×10^{-5}	7.08×10^{-2}
CXB + GCR(5)	1.53×10^{-2}	26.9
CXB + GCR(6)	1.53×10^{-2}	26.8
CXB + GCR(7)	1.52×10^{-2}	26.7

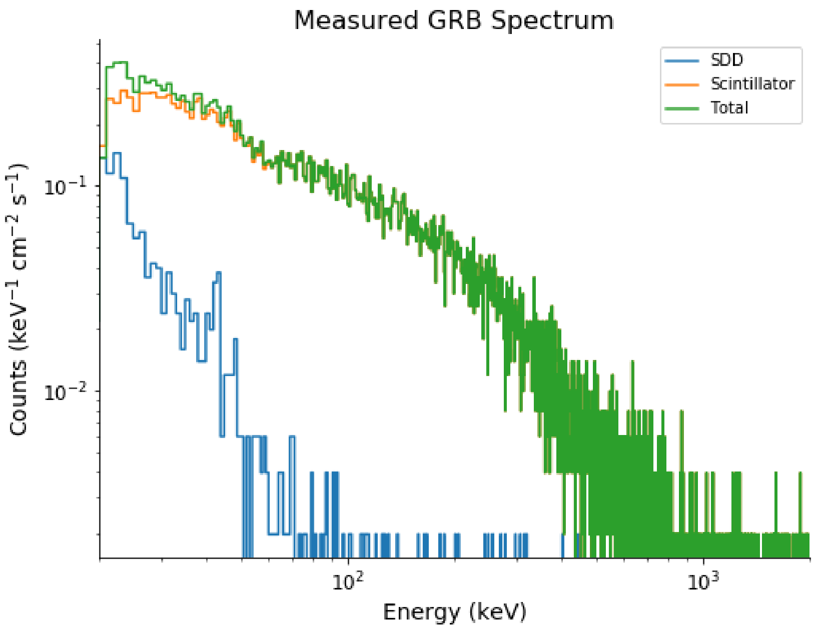

Figure 4.18: Result of simulating a GRB. The single components measured by the SDDs (blue) and the scintillator crystals (orange) are shown together with their sum (green), which represents the total measured photon flux of the GRB.

In order to get a complete impression of the measured spectrum of a GRB observation, the background flux must also be taken into account. Therefore, the measured GRB spectrum was added to the detector background and plotted together with the single components in Figure 4.19. Since the background spectra induced by the different GCR models are similar, the resulting spectrum of only one model (CREME96 and Smart & Shea shielding) is used to obtain the total measured spectrum. Both orbits were analyzed to obtain possible differences. Table 4.5 allows to compare the results on the basis of the calculated average differential fluxes and total fluxes. It can be seen that there is no significant difference between the observations from the different orbits and that the spectrum of the GRB can be measured in the same clear way. Note that the energy range starts at 20 keV because the simulated GRB spectrum begins at this photon energy.

4.5 Conclusion

The Monte Carlo simulation studies for the determination of the HERMES detector background show that the dominant contribution is generated by the photons of the cosmic X-ray background. This part of the detector background spectrum has a very high flux especially towards lower energies. The protons of the galactic cosmic rays have a weaker impact on the detector background. Their contribution varies with the satellite's orbit. In an orbit with low inclination the detector background induced by the protons is lower than in the high inclination orbit. How strongly this component of the detector background varies between the orbits depends on the chosen magnetic shielding model. Since the CXB induced component dominates the detector background, the differences between both orbits become negligible in the total detector background.

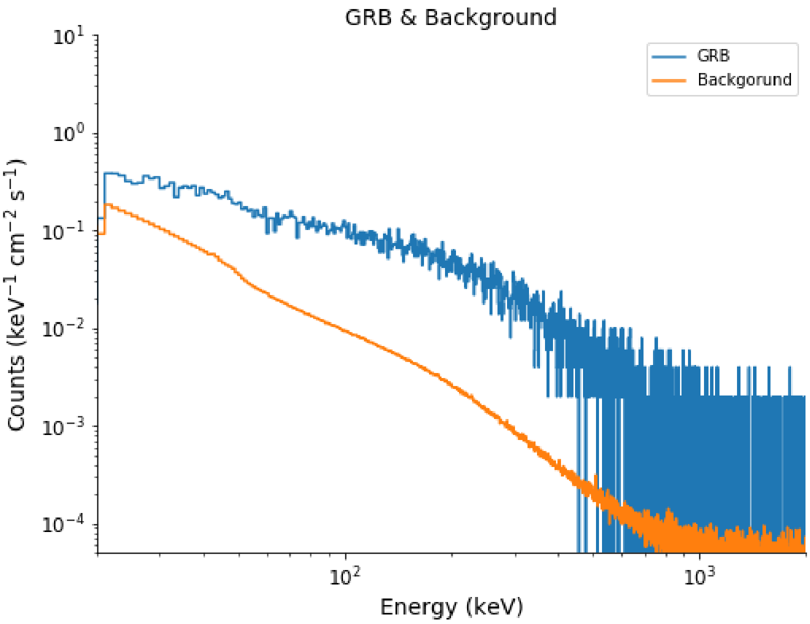

Figure 4.19: The measured GRB spectrum (blue) in comparison to the detector background (orange), which is simulated with the CREME96 model and the Smart & Shea shielding for the high inclination orbit.

Table 4.5: The average differential flux and the total flux of the spectra resulting from the GRB simulation. First, the values for the GRB events, followed by the values for the total spectra where the GRB events are added to the background events (BKG = GCR with CREME96 model with Størmer shielding + CXB). These calculations were done for the low and the high inclination orbit.

Model	Average Differential Flux in counts/(s cm^2 keV)	Total Flux in counts/(s cm^2)
GRB	1.42×10^{-2}	28.4
GRB + BKG (2.5°)	2.947×10^{-2}	55.16
GRB + BKG (57°)	2.950×10^{-2}	55.20

To compare the detector background with an observed source, an observation of a gamma-ray burst was simulated. The detected GRB spectrum ranges from 20 keV to 2 MeV. Up to energies of about 500 keV, the detected flux is significantly higher than the detector background flux, regardless of the orbit.

Chapter 5

Conclusions

In the framework of this thesis, Monte Carlo simulations were performed using the simulation toolkit Geant4 to predict the detector background of the future X-ray telescopes eXTP and HERMES in their orbits in space.

The simulation environment was set to generate an isotropic flux of photons coming from the cosmic X-ray background and the galactic cosmic rays (GCR, protons of galactic origin) that contribute to the detector background. The Large Area Detector (LAD) on-board the eXTP satellite was subject of the simulation studies, for which the geometry of one LAD module was implemented in the Geant4 simulation code. An already existing geometry including the HERMES satellite structure and the detector module created by R. Campana was used for the HERMES simulations.

The simulations indicated an average differential LAD background flux between 3.31×10^{-4} and 3.71×10^{-4} counts $(\mathrm{s\,cm^2\,keV})^{-1}$ depending on the chosen GCR model. The corresponding total fluxes are 2.58×10^{-2} and 2.89×10^{-2} counts $(\mathrm{s\,cm^2})^{-1}$ over the entire energy range of 2 - 80 keV covered by the LAD. It was also checked whether the specification of a detector background below 10 mCrab, as stated by Zhang et al. (2019), is met. The simulation studies showed that the determined background is below this value and therefore the requirement is fulfilled.

The detector background simulation studies of HERMES revealed an average differential flux of $\sim 1.53 \times 10^{-2}$ counts $(\mathrm{s\,cm^2\,keV})^{-1}$ and a total flux of ~ 26.8 counts $(\mathrm{s\,cm^2})^{-1}$ that do not change significantly due to the different GCR models or orbits. This is because the CXB has a very strong impact on the detector background such that the contribution of the GCR component is almost negligible. To predict the scientific performance, a source observation was simulated as well. For this, photons of a gamma-ray burst spectrum were simulated and the measured spectrum was compared and combined with the detector background. This showed that the measured GRB spectrum stands out significantly from the detector background and is clearly observable.

In the simulation studies in this work only the CXB and the GCR protons were considered. Since there are more components contributing to the detector background, further studies could also consider additional sources, such as trapped particles to determine the detector background more accurately. Furthermore, the geometry of the satellite could be reproduced even more detailed and on a wider scale.

With the current simulation environment, tests can be performed to find possibilities to reduce the background even further by varying the geometry, for example by using different materials or changing dimensions of components. Additional shielding could also help to reduce the detector background.

This work enabled a prediction of the detector background that can be expected for future observatories and provides a complete simulation environment for further simulation studies.

Bibliography

Agostinelli, S., Allison, J., Amako, K., et al. 2002, Nuclear Instruments and Methods in Physics Research Section A: Accelerators, Spectrometers, Detectors and Associated Equipment, 506, 250

Band, D., Matteson, J., Ford, L., et al. 1993, Astrophysical Journal, 413, 281

Campana, R., Feroci, M., Del Monte, E., et al. 2013, Experimental Astronomy, 36, 451

Courvoisier, T. J.-L. 2013, High Energy Astrophysics - An Introduction (Springer)

De Rosa, A., Uttley, P., Gou, L., et al. 2019, Science China Physics, Mechanics, and Astronomy, 62, 29504

Feroci, M., Ahangarianabhari, M., Ambrosi, G., et al. 2018, in Society of Photo-Optical Instrumentation Engineers (SPIE) Conference Series, Vol. 10699, Space Telescopes and Instrumentation 2018: Ultraviolet to Gamma Ray, 106991C

Fraser, G. W. 1989, X-ray detectors in astronomy

Fuschino, F., Campana, R., Labanti, C., et al. 2018, arXiv e-prints, arXiv:1812.02432

Gilli, R., Comastri, A., & Hasinger, G. 2007, Astronomy and Astrophysics, 463, 79

Gruber, D., Goldstein, A., Weller von Ahlefeld, V., et al. 2014, Astrophysical Journal Supplement, 211, 12

Gruber, D. E., Matteson, J. L., Peterson, L. E., & Jung, G. V. 1999, Astrophysical Journal, 520, 124

Harrison, R. L. 2010, AIP Conference Proceedings, 1204, 17

Kaneko, Y., Preece, R. D., González, M. M., Dingus, B. L., & Briggs, M. S. 2005, Washington DC American Geophysical Union Geophysical Monograph Series, 156, 275

Kirsch, M. G., Briel, U. G., Burrows, D., et al. 2005, in Society of Photo-Optical Instrumentation Engineers (SPIE) Conference Series, Vol. 5898, UV, X-Ray, and Gamma-Ray Space Instrumentation for Astronomy XIV, ed. O. H. W. Siegmund, 22–33

Mikaelian, T. 2009, arXiv e-prints, arXiv:0906.3884

Nymmik, R., Panasyuk, M., & Suslov, A. 1996, Advances in Space Research, 17, 19

Ross, E. & Chaplin, W. J. 2019, Solar Physics, 294, 8

Santangelo, A., Zane, S., Feng, H., et al. 2019, Science China Physics, Mechanics, and Astronomy, 62, 29505

Schaefer, B. E., Palmer, D., Dingus, B. L., et al. 1998, The Astrophysical Journal, 492, 696

Seitz, B., Campos Rivera, N., & Stewart, A. 2016, IEEE Transactions on Nuclear Science, 63, 503

Shea, M. A. & Smart, D. F. 1967, Journal of Geophysical Research, 72, 2021

Staubert, R., Trümper, J., Kendziorra, E., et al. 2019, aap, 622, A61

Störmer, C. 1930, Zeitschrift für Astrophysik, 1, 237

Sullivan, J. D. 1971, Nuclear Instruments and Methods, 95, 5

Topinka, M. 2009, Baltic Astronomy, 18, 271

Tylka, A. J., Adams, J. H., Boberg, P. R., et al. 1997, IEEE Transactions on Nuclear Science, 44, 2150

Watts, A. L., Yu, W., Poutanen, J., et al. 2019, Science China Physics, Mechanics, and Astronomy, 62, 29503

Zhang, S., Santangelo, A., Feroci, M., et al. 2019, Science China Physics, Mechanics, and Astronomy, 62, 29502

Acknowledgments

Ich möchte mich bei allen Personen, die mich während meiner Masterarbeit unterstützt haben, ganz herzlich bedanken.

Zuerst möchte ich Prof. Andrea Santangelo für die Möglichkeit danken, meine Masterarbeit in der Arbeitsgruppe für Hochenergieastrophysik zu schreiben.

Sehr dankbar bin ich für die großartige Unterstützung von Dr. Chris Tenzer, für seine hervorragende Betreuung meiner Masterarbeit, für das Korrekturlesen und seine Hilfe bei allen aufkommenden Fragen.

Stephanie Klein danke ich für das Korrekturlesen meiner Arbeit.

Meinen Kommilitonen im Büro und den Mitarbeitern der Arbeitsgruppe möchte ich für die schöne gemeinsame Zeit danken.

Ganz besonders möchte ich mich noch bei meiner Familie, vor allem bei meiner Mama und meinem Bruder, bedanken. Danke, dass ihr mich immer unterstützt und für mich da seid.

Meinem Freund möchte ich von Herzen für seine Unterstützung und Rücksicht während meines Studiums und besonders während dieser Masterarbeit danken. Nico, ich bin sehr froh, dass du in meinem Leben bist.

Marina, Leon und Felix, ich danke euch für die wundervolle Studienzeit und hoffe auf viele weitere schöne gemeinsame Momente.